A study to end-winding induced iron losses in high-speed electrical machines with concentrated windings

T. Feenstra

Technische Universiteit Delft

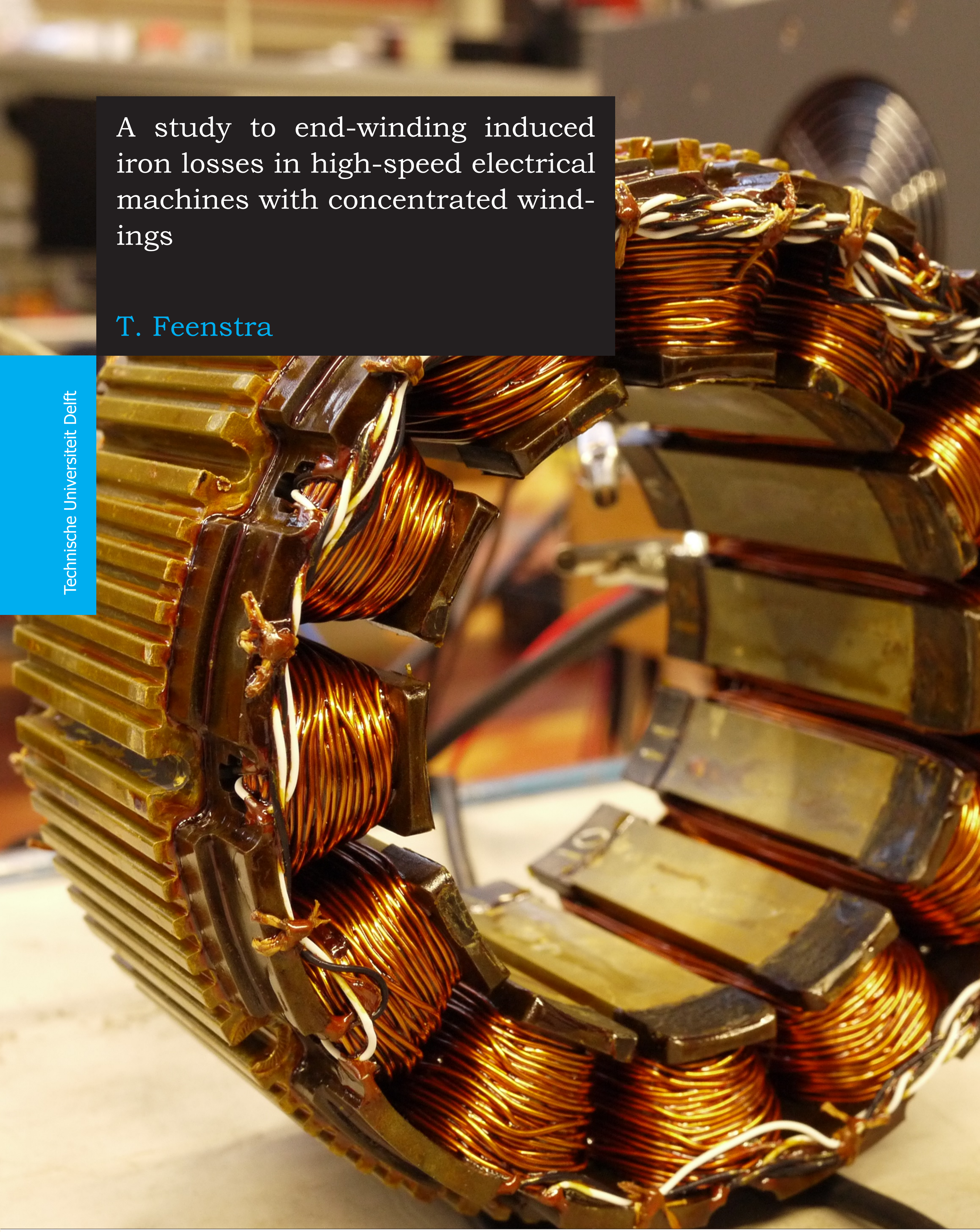

Delft University of Technology

Challenge the future

A study to end-winding induced iron losses in high-speed electrical machines with concentrated windings

by

T. Feenstra

in partial fulfillment of the requirements for the degree of

Master of Science
in Electrical Engineering

at the Delft University of Technology,
Faculty of Electrical Engineering, Mathematics and Computer Science,
Department of Electrical Sustainable Energy,
to be defended publicly on Tuesday December 13, 2016 at 3:00 PM.

T. Feenstra
Studentnr: 1524194
timfeenstra90@gmail.com

Supervisor:	Dr. ir. H. Polinder,	TU Delft
Thesis committee:	Dr. D. J. P. Lahaye,	TU Delft
	J. Dong,	TU Delft

Abstract

One potential problem associated with the high electrical frequency in high-speed electrical machines are additional iron losses near the end-windings. They are expected to be a significant part of the total iron loss. The reader is introduced to currently known methods to study high-frequency iron loss estimation and end-effects in laminated media. No suitable method is found. Therefore, an experimental approach is presented. A short-axial laminated stator core is exposed to high-frequency excitation fields generated by coils with normal and extended end-winding heights. The proposed experimental method is verified numerically with a simplified brute-force 3D finite element model. Significant less losses are measured and calculated for the extended end-winding case. Non-homogeneous material properties in the core also seems to influence the measured iron losses at higher frequencies. The results show that most of the high-frequency losses are induced in the stator end laminations near the end-winding. In addition, it is found that the traditional eddy-current model underestimates the modelled results significantly if a wrong peak magnetic flux density is used. With both the experimental and numerical approach, it is shown that the impact of high-frequency end-winding induced iron losses on the total core loss cannot be neglected in iron loss estimation methods for short axial high-speed electrical machines with concentrated windings.

Preface and acknowledgement

This thesis work is carried out at Delft University of Technology, in the department of DC systems, Energy conversion & Storage (DCES). The topic was provided by Dr. ir. M. van der Geest, who was doing research to high performance permanent magnet synchronous machines at that moment. It was an interesting topic, mainly because I was able to do some practical work. I would like to thank my supervisors Dr. ir. H. Polinder and Dr. ir. M. van der Geest for supporting me during this project.

Finishing this thesis work was not an easy process for me. However, with the support of my family, friends, and colleagues I finally did it. I would like to thank all people who pushed me to finish this work.

Finally, I would like to give a special thanks to my parents for their continuous support and faith in me.

T. Feenstra
Amsterdam, November 2016

Contents

List of Figures

List of Tables

1
Introduction

1.1. background

High-speed electrical machines (HSEMs) have been getting a lot of interest in the last couple of years, partly due to improvements in the enabling technology and partly due to the high potentials these machines have. Advantages such as increased power density, reduced volume and weight, and lower costs make HSEMs attractive for many applications. For example, HSEMs are already used in compressors, drilling tools, turbine generators, turbochargers, helicopter and racing engines, and so on. In many application areas, researchers are pushing their research toward improvements in the involved HSEMs technologies, which involves many challenges that need to be considered. These include higher losses per volume, fringing effects and cooling considerations [1][2].

In this trend towards lighter, more power dense electromechanical systems, the rotational speed -and with that the electrical frequency- of electrical machines is increasing. Typical speeds are over 10000 rpm and applications with speeds of up to 150000-200000 rpm are already under consideration [3]. The electrical frequency is further increased by the use of concentrated windings with high pole counts, which are more attractive than distributed windings due to their reduced end-winding volume and simpler fabrication process [4]. In addition, increasing machine speeds often imply shorter axial lengths, increasing the impact of end-effects on the machine performance. Useful techniques have been developed for investigating the complex end-effects in electrical machines [5][6][7]. However, most of them do not apply to HSEMs in their current form [8].

Additional core loss near the end-windings is such an end-effect. Several studies dedicated to rotating electrical machinery have shown that additional eddy currents are induced in the stator teeth due to the axial flux, especially in the end laminates of the stator stack. This axial flux is mainly induced by the end-windings and has an alternating component perpendicular to the lamination direction. Those studies focus mainly on large turbo generators operating at 50 or 60 Hz and leave room for research focusing on HSEMs.

1.2. Problem definition

One potential problem associated with the high electrical frequency is additional core losses near the end-windings, due to the non-ideal orientation of the end-windings to the stator laminations. Figure 1.1 shows the anticipated problem areas for a surface permanent magnet (SPM) machine with an outer stator and concentrated windings. The problem statement is defined as follows:

What is the impact of end-winding induced iron losses on the total core losses in high-speed electrical machines with concentrated windings?

In this work it is assumed that all the magnetic field waveforms are sinusoidal. Complex non-sinusoidal waveforms with higher time harmonics or arbitrary waveforms are beyond the scope of this Thesis.

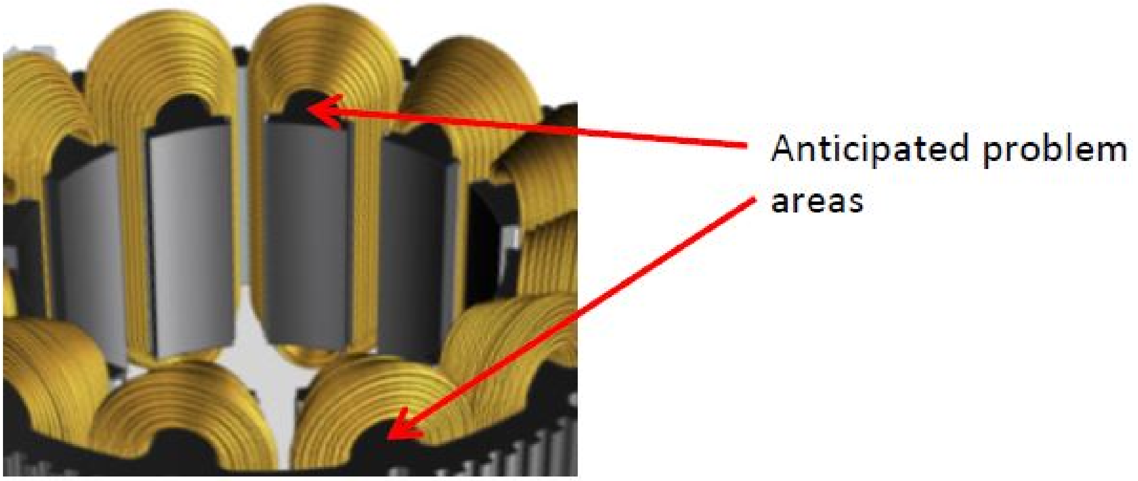

Figure 1.1: Anticipated problem areas of end-winding induced iron losses

1.3. Research objectives

The research objectives are as follows:

1. A literature review on high-frequency end-winding induced iron losses.
2. Build an experimental setup and measure end-winding induced core loss in a laminated stator core.
3. Development of a simplified 3D end-winding model with a commercial FEM package.
4. Simulate the the impact of end-winding induced iron losses on the total core losses.

1.4. Thesis outline

To get to the conclusion of this Thesis, chapter 2 will start with a literature review on high-frequency end-winding induced core losses in laminated media. Experimental results regarding end-winding induced iron losses in an actual stator are covered in chapter 3. In chapter 4, a simplified 3D FEM model is build to study end-winding incuded eddy-current losses. Finally, the conclusion is provided in chapter 5.

2

End-winding induced iron losses

Chapter 2 aims

- To describe and evaluate known methods for determining high-frequency iron losses in steel laminations.
- To describe and evaluate existing scientific literature that have been used for the analysis of end-winding induced iron losses.

This chapter involves a review of the scientific work done concerning end-winding induced iron losses in magnetic cores. First, a brief introduction to end-winding induced iron losses is given in Section 2.1. Section 2.2 will review existing methods to estimate iron losses at high excitation frequencies. Finally, Section 2.3 will conclude this chapter with the method that is going to be used in this Thesis to analyse the end-winding induced iron losses.

2.1. Introduction to end-winding induced iron losses

To reduce eddy-current losses, stator cores of electrical machines are stacked with steel sheet laminations separated by an insulation layer. They are designed in such a way that the laminations are parallel to the main magnetic field. However, there are also unavoidable magnetic leakage fields, particularly in the end-region. The leakage field due to the end-winding has a considerable normal component with respect to the end-laminations, resulting in additional current loops parallel to sheets. The induced eddy-current loops due to the magnetic main field (B_m) and end-winding leakage field (B_p) are visualised in Figure 2.1. The in-plane eddy-currents i_p that are induced in the steel may increase the temperature in the stator core, which influence the machine characteristics in a negative way.

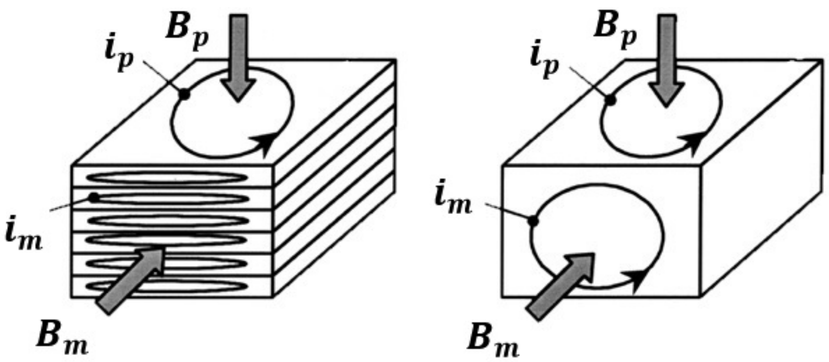

Figure 2.1: Eddy-current loops in a laminated iron core (left) and a solid iron core (right)

All reported analysis on eddy currents in core ends are focusing mainly on low-speed large-sized turbo generators operating at 50 or 60 Hz [9][10][11]. It is shown that the loss due to axial flux is small in comparison with the total iron loss. However, they can be big enough to generate local hot spots in the laminations [12]. No analytical methods exist that include end-winding induced iron losses in the estimation of the total core loss. However, several 2D and 3D numerical models to include the end-winding induced iron losses are proposed. Those methods will be discussed in Section 2.2.3. First, 1D analytical iron loss models are discussed to gain more insight in the behaviour of high-frequency iron losses in the laminated media.

2.2. Analytical iron loss models for laminated media

Traditionally, the total iron loss P_t is calculated by adding the static hysteresis loss P_h to the dynamic eddy-current loss P_e. For sinusoidal magnetic flux waveforms, the total iron loss is given by

$$\begin{aligned} P_t &= P_h + P_e \\ &= k_h f \hat{B}^n + k_e f^2 \hat{B}^2 \end{aligned} \tag{2.1}$$

where:

f = Excitation frequency
$\hat{B}$ = Maximum flux density
n = Steinmetz constant; material dependent
k_h = Hysteresis loss coefficient
k_e = Eddy current loss coefficient

Equation 2.1 is not completely satisfactory. The measured losses are much greater than theoretically calculated. A lot of effort is made to explain those excess losses [13][14][15][16]. The most accepted and adopted theory is introduced by Bertotti. He introduced an additional excess loss component P_{ex} to equation 2.1, which represents microscopic eddy current loss caused by domain wall movement. The iron loss is given by

$$\begin{aligned} P_t &= P_h + P_e + P_{ex} \\ &= k_h f \hat{B}^n + k_e f^2 \hat{B}^2 + k_{ex} f^{1.5} \hat{B}^{1.5} \end{aligned} \tag{2.2}$$

where k_{ex} is the excess loss coefficient. The loss seperation approach is in good agreement with several loss experiments, but it does not seem to be sufficiently general.

The coefficients in equation 2.2 are generally obtained from the measured core loss data and are assumed to be constant values. However, several researchers found that the coefficients vary with frequency and flux density [17][18][19][20], resulting in

$$\begin{aligned} P_t &= P_h + P_e + P_{ex} \\ &= k_h(f,\hat{B}) f \hat{B}^{n(f,\hat{B})} \hat{B}^{1.5} + k_e(f,\hat{B}) f^2 \hat{B}^2 + k_{ex}(f,\hat{B}) f^{1.5} \hat{B}^{1.5} \end{aligned} \tag{2.3}$$

Although equation 2.3 is more accurate, it requires additional core loss data at high frequencies and high flux densities to determine the variable coefficients. If the necessary data is not provided by the steel manufacturer, the data is normally obtained with an Epstein frame. Due to the fact a lot of data is needed, the modified equation is not used a lot in literature yet. More studies are needed to use the modified core loss model in practical designs for HSEMs.

Equation 2.2 is widely used because it results in the total loss per unit mass. However, it does not take into account machine dimensions. A few studies introduced methods to take into account machine dimensions in iron loss modeling for a SPM machine [21][22][23]. They proposed to split the losses into yoke (y) losses and teeth (t) losses:

$$P_t = P_{ht} + P_{hy} + P_{et} + P_{ey} \tag{2.4}$$

where h stands for hysteresis and e for eddy current. It is given that only the eddy-current loss is dependent on the lamination shape, the hysteresis losses can still be approached by the Steinmetz equation. Iron loss models that take into account machine dimensions are relatively new and will not be considered in this Thesis.

The most common analytical models that are used to estimate iron losses have been discussed in this section. They are only accurate for sinusoidal excitation within a certain frequency and flux density range. In addition, there are no methods to measure the loss components in equation 2.2 individually at a given frequency f. However, other methods are used to determine the loss components. The static hysteresis loss, P_h, is usually obtained from the area closed by the hysteresis loop measured at low frequency, say 1-5 Hz, or by extrapolating the total measured loss to zero frequency. The eddy-current loss, P_e, is estimated analytically or with finite element modelling. Finally, the excess loss, P_{ex}, is calculated by subtracting P_h and P_e from the measured total loss, P_t.

At high electrical frequencies, the eddy-current losses and the excess losses will dominate the iron losses, as they are proportional to f^2 and $f^{1.5}$, respectively. According to Zirka, a 10% error in the calculated classical loss at 1.5T results in errors of 25 and 50% in excess loss at 50 and 100 Hz, respectively [24]. Calculating the eddy-current loss component correctly is expected to be important for iron loss estimation in HSEMs. Next subsection will discuss analytical and numerical methods to calculate the eddy-current loss component at high electrical frequencies.

2.2.1. 1D approach to model eddy-current losses

For a low-frequency sinusoidal varying magnetic field, the eddy-current loss per unit volume in laminated steel is approximated by the well known equation

$$P_e = \frac{\sigma\pi^2 d^2}{6} f^2 \hat{B}^2 \tag{2.5}$$

where σ is the conductivity of the magnetic material and d is the lamination thickness. It is usually neglected that equation 2.5 is derived for linear dependent $B(H)$ ferromagnetic materials and is only valid for frequencies where skin-effect is negligible. This is the main reason for inaccuracy of the loss separation carried out analytically for non-oriented electrical steel. Gyselinck showed that for frequencies up to 50-60 Hz equation 2.5 is accurate enough [25]. However, to be more accurate at higher frequencies, the full form of equation 2.5 should be considered [26].

$$P_e = \frac{\sigma\pi^2 d^2}{6} f^2 \hat{B}^2 F(\gamma) \tag{2.6}$$

Here the skin-effect function $F(\gamma)$ is

$$F(\gamma) = \frac{3(\sinh\gamma - \sin\gamma)}{\gamma(\cosh\gamma - \cos\gamma)} \tag{2.7}$$

where $\gamma = d/\delta$ and δ is the skin depth and results from the skin-effect; the phenomenon where electromagnetic fields (and therefore the current) decay rapidly with depth inside a good conductor. This depth is given as

$$\delta = \sqrt{\frac{1}{f\pi\mu\sigma}} \tag{2.8}$$

and describes the length of penetration over which the magnitude of the field decays to $1/e$. At high electrical frequencies, the flux density in the center of the lamination reduces as skin effect becomes significant.

More recently, another eddy-current loss equation taking into account the skin effect is developed. To take into account the new flux distribution in the lamination at higher frequencies, Mthombeni [27] proposed to rewrite equation 2.5 to

$$p_e = k_e f^2 \hat{B}^2 = \sigma\pi^2 f^2 \hat{B}^2 K_{sk}, \tag{2.9}$$

with

$$K_{sk} = \left(\frac{\delta \left(e^{-\frac{2\delta - d}{\delta}} - e^{2} \right)}{e^{\frac{d}{\delta}} + 1} \right)^{2} \tag{2.10}$$

Equation 2.9 basically means that, according to K_{sk}, the material thickness d "reduces". Equation 2.9 is not yet widely used the field of iron loss calculation and should be validated first.

Using fine-element modelling (FEM), Brauer tested the validity of equation 2.5 for two laminations separated by a thin insulation layer (air) [28]. For low frequencies, where the skin depth is much greater than lamination thickness, equation 2.5 is used. For high frequencies (10 kHz or higher), where the skin depth is much less than metal thickness, a loss formula used by radio engineers' is used. The eddy-current loss per unit area at high frequencies is given as follows:

$$P_e = \frac{1}{2} |H_{tan}|^2 R_s \tag{2.11}$$

where H_{tan} is the peak tangential incident magnetic intensity and R_s is the surface impedance in ohms per square meters. R_s is, in turn, related to skin depth δ by $R_s = \frac{1}{\delta\sigma}$. The formula is not yet used for eddy-current loss estimation in electrical machines. However, with frequencies getting higher this might be interesting for later.

Although the discussed equations can approximate the eddy-current losses fast for most problems, there are still some issues.

1. They are derived for simple geometries such as transformer cores. The geometry of stator cores in electrical machines are much more complex. This is shown in Figure 2.2 and Figure 2.3;
2. They assume an uniform magnetic field parallel to the surface of the lamination. However, in the end-laminations there is a non-uniform magnetic field induced by the end-windings;
3. They do not take into account the 3D eddy-current distribution inside each lamination and the effect of the magnetic field induced by those 3D eddy-currents on nearby laminations;
4. They are not valid for non-linear materials due to the fact that the magnetic permeability μ is kept constant.

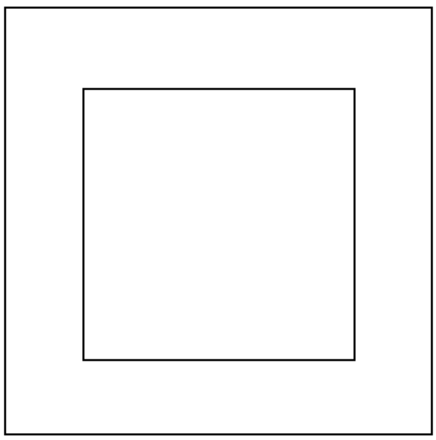

Figure 2.2: Simple 2D geometry of a transformer core

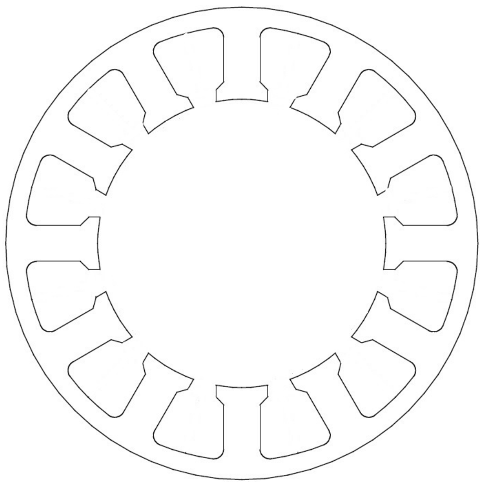

Figure 2.3: Complex 2D geometry of a stator core

2.2.2. 2D approach to model eddy-current losses

To take into account the magnetic flux density distribution in the complex geometry of stator cores, engineers were forced to use the finite element method. The method will be discussed in detail in Chapter 4. In short, it subdivides a large problem into smaller, simpler parts that are called finite elements. Simple equations can be applied to those finite elements to determine, for example, the eddy-current loss distribution of the defined problem.

The 2D FE method can be enhanced by including eddy-current [29] or hysteresis and excess effects [30][31]. Over a wide range of frequencies, this method gives a rough approximation of the total losses if the FEM problem is defined correctly. The drawback of this 2D-FEM method is that it ignores the local electromagnetic field distribution inside each lamination. In addition, it also neglects the effect of the end-winding. 3D approaches are proposed to study those effect.

2.2.3. 3D approach to model eddy-current losses

The best way to model the three-dimensional (3D) eddy current distribution is by modelling each lamination of a magnetic core individually. However, this would require a large finite element model leading to large systems of equations. Limited literature is available about the simulation of the eddy-current field distribution in the end lamination, especially for HSEMs. To get a better understanding of the development of such a model, a brief history of modelling eddy-currents in laminates is given.

To simplify the problem, homogenization techniques were introduced by representing the magnetic core as a bulk medium. In early finite element methods, the laminar eddy current distribution parallel to the lamination is obtained by describing a current vector potential having a single component normal to the lamination [32] or by applying an anisotropic electric conductivity [33]. The latter method is the most flexible and sets the value of electric conductivity in the lamination direction to zero or very low. If the stack is laminated in the z direction, the conductivity matrix $[\sigma]$ is given as

$$[\sigma] = \begin{bmatrix} \sigma_x & & \\ & \sigma_y & \\ & & \sigma_z \end{bmatrix} = \begin{bmatrix} F\sigma & & \\ & F\sigma & \\ & & 0 \end{bmatrix} \tag{2.12}$$

where F is the stacking factor of the laminated core. The anisotropic methods describes the magnetic flux distribution in the magnetic core well. However, it fails to calculate the correct eddy current distribution in each lamination for frequencies where skin effect is pronounced. In addition, it neglects the main magnetic field parallel to the lamination direction [34]. To solve this, several correction methods for linear and nonlinear materials have been introduced, including 1D [35][36][37] and 3D correction methods [34][38]. The 1D correction methods neglect edge effects and is not valid anymore for small machine parts such teeth (tips), bridges or closed slots [39][40].

In aforementioned methods, the eddy currents distribution in the laminates due to the main flux and the stray flux is treated separately. However, in reality they influence each other and make above methods inaccurate, especially for non-linear materials [41]. To calculate the static 3D magnetic field directly, the use of a magnetic scalar potential [42], a magnetic vector potential [43] or a second-order vector potential is proposed [44][45][46]. The calculated static 3D magnetic field is used to obtain the eddy current distribution in the laminates [47]. This method assumes a symmetric magnetic flux density across the laminates. This is not the case at the end winding region of a lamination stack, so a solution to this problem was proposed by [48]. To also take into account the insulation between the lamination, mostly simulated as air, the use of a two-scale finite element method (TSFEM) was proposed for linear materials [41], and later for nonlinear materials [49].

Other methods to approximate the real eddy current distribution is to model at least four end-laminations individually and the middle laminates as a bulk medium with anisotropic conductivity [50]. Also methods that couples an overall 3D model and the 2D or 3D model of an individual lamination are proposed [7][51]. The calculated loss of one lamination is multiplied by the amount of laminates in the stator stack. This method does not take into account the end-effects and the effect of the laminates on each other. An alternative to this method is proposed by coupling an overall 3D model to 2D slice models which account for the complicated eddy-current path perpendicular to the lamination direction [52]. Finally, a more advanced anisotropic method taking into account the eddy currents in laminates inherently seems to work well for frequencies up to 100 kHz [53]. However, edge effects must be negligible, which is not the case in stator teeth of HSEMs.

The proposed 3D methods are all simplifications of the real 3D eddy-current problem. Applying homogeneous methods greatly helps to reduce the computing time. The methods can estimate the iron losses well for frequencies where skin effect is negligible. This is not the case in HSEMs. To effectively study the effect of end-winding induced eddy-current losses for higher excitation frequencies, all the laminations must be modelled individually in 3D.

2.3. Chapter conclusion

It can be concluded that at medium frequencies no simple iron loss estimation methods apply. Deriving a formula that takes into account the effect of end-winding induced iron losses in HSEMs will be very complex. It is noticed that the hysteresis loss and excess loss cannot be neglected in iron loss estimation. However, as the eddy-current are proportional with f^2, the focus of iron loss estimation in HSEMs is on calculating the eddy-current loss. The analytical eddy-current estimation methods do not take into account the skin effect and the non-uniform magnetical field in the core ends due to the end-winding. This forces most engineers to use the finite element method to estimate the iron losses.

At high frequencies, the skin effect plays an important role in estimating the iron losses. The eddy-currents will cluster at the edges of te lamination. However, no fully accepted finite element method is yet developed to take into account the skin effect. To fully understand the effect of end-winding induced iron losses in laminated cores a 3D FEM model needs to be built where the laminations will be evaluated individually, especially in the skin depth area. In chapter 4, such a model is built and analysed.

3

Experimental testing

Chapter 3 aims

- To build an experimental setup and measure the impact of end-winding induced iron loss on the total core loss in a laminated stator core.

A method to analyse the impact of end-winding induced iron loss on the total core loss is presented in section 3.1. In section 3.2, the results are presented and discussed. The chapter conclusion is given in section 3.3.

3.1. Measurement method

Methods to measure the total core loss include thermal or electric power measurements. The former measures the power dissipated by the system; the latter measures the power consumed by the system. For both methods, it is hard to tell which part is hysteresis, eddy-current or excess loss. Differentiate the in-plane eddy-current loss from the total core loss is even more difficult. A few devices to that attempt to measure and analyse the in-plane eddy current in large turbo generators are introduced [9][10][11]. Unfortunately, those methods are relatively complex and most of the required equipment is not available for this research. Design and build our own in-plane eddy-current tester for end-winding losses is expensive and time consuming, and is therefore not considered as an option.

At its simplest form, only considering a stator and its coils, the total loss in the system can be subdivided into copper losses and iron losses. If the total losses and the copper losses are known, the iron losses in the stator can be studied specifically. This makes it possible to observe change in the measured iron losses while varying physical system parameters; parameters that are expected to influence the end-winding induced iron losses. If a notable change is observed, there is a possibility that this is caused by increasing or decreasing end-winding induced iron losses.

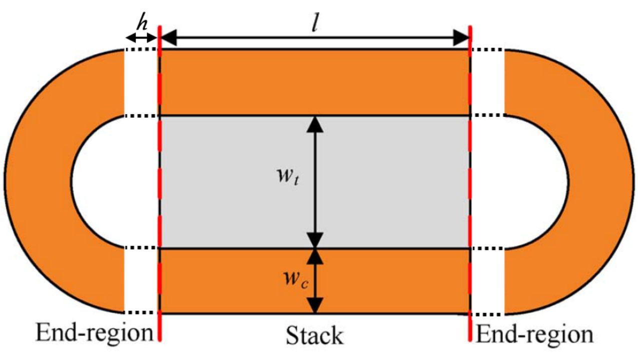

Figure 3.1: Top view of a concentrated winding

Figure 3.1 shows the top view of a concentrated winding. The coil dimensions that can be altered are the stack length l, the tooth width w_t, the coil width w_c, the coil depth w_d, and the end-winding height h. It is noticed that the end-winding can also have other shapes than circular, i.e. squared or triangular. However, it is preferred to avoid sharp corners to avoid damaged wires and concentrated electric fields.

For a coil that is tightly wound around its stator tooth, the magnetic field near the end-winding is not able to close its path through air. This forces the end-winding field to penetrate the steel laminations in laminar direction, and induces in-plane eddy-currents. According to this, it would make sense to look at the effect of altering the end-winding height h. Increasing the end-winding height results in additional vacant space between end-winding and the stator teeth. More field lines are expected to close without penetrating the stator core, lowering the end-winding induced iron loss in the stator laminations.

Reference measurements will be done to measure the iron losses due to the magnetic field induced by a coil tightly wound around a stator tooth. The amount of iron losses induced by the end-winding is expected to be greatest in this reference situation. Next, the iron losses due to the magnetic field induced by a coil with elevated end-windings is measured. The results are compared, such that the impact of the end-winding induced iron losses can be studied.

The proposed method can give more insight into the impact of end-winding induced iron loss to the total iron loss at several frequencies and magnetic field strengths. However, it is noticed that with this method it is impossible to differentiate between those losses.

3.1.1. Experimental setup

To focus only on the iron losses, a single stator stack with electrical steel sheets is used. The stator dimensions and the specifications of the core material are given in Table 3.1. The $B(H)$ curve is not available for the test sample. However, the excitation currents on the coils will be low enough to assume that the magnetic field will stay in the linear part of the curve. The single stator stack and a top view of the stator is shown in Figure 3.2 and Figure 3.3, respectively.

Table 3.1: Details of the experimental stator

(a) Core dimensions

Geometry parameter	Value
Stator outer radius (mm)	67
Yoke Thickness (mm)	5.34
Tooth width (mm)	10.25
Stator inner bore (mm)	40.88
Stack length (mm)	47.76
Shoe height (mm)	3.2
Shoe span at inner bore	69.7%

(b) Specifications of the core material

Material property	Value
Grade	M270-35A
Thickness (mm)	0.35
Stacking factor	0.95
Conductivity σ (S/m)	1.923x10^6

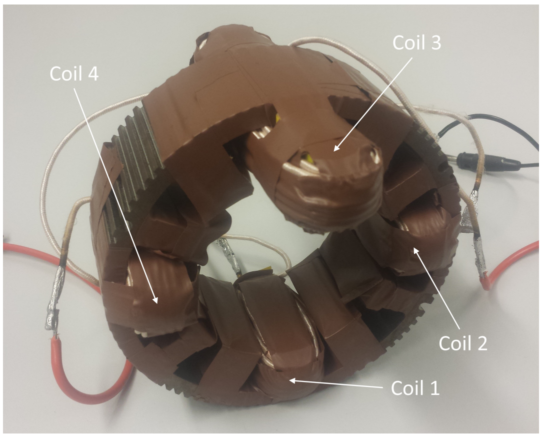

Figure 3.2: Test stator with four windings

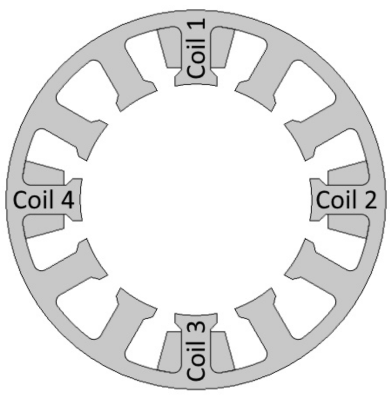

Figure 3.3: Top view of the stator

To prevent a short circuit between the coils and the electrical steel, the stator core is insulated with electrical insulation tape. Four coils with eighteen turns ($N = 18$) are wound around teeth that are separated ninety degrees from each other. This is because material properties of the steel lamination can be influenced by the manufacturing process. This is proven for the rolling direction of the steel sheets [54]. Opposing teeth have the same rolling direction, so it is assumed the material properties are the same in those teeth. In this setup the iron losses due to reference coil 1 can be compared with those of coil 3. The same applies to reference coil 2 and coil 4.

The end-winding length in coil 3 and coil 4 are elevated by using different spacers made of wood and PVC, see Figure 3.4. The length of the end-winding of coil 3 is chosen to be relatively large to make sure that end-winding effects will have limited effect on the iron losses in the stator core. Coil 1 and Coil 2 have the same dimensions and are tightly wound around the stator tooth. The end-winding height of coil 4 is only supported by a piece of PVC. The coils are hold in place with electrical tape as shown in Figure 3.5.

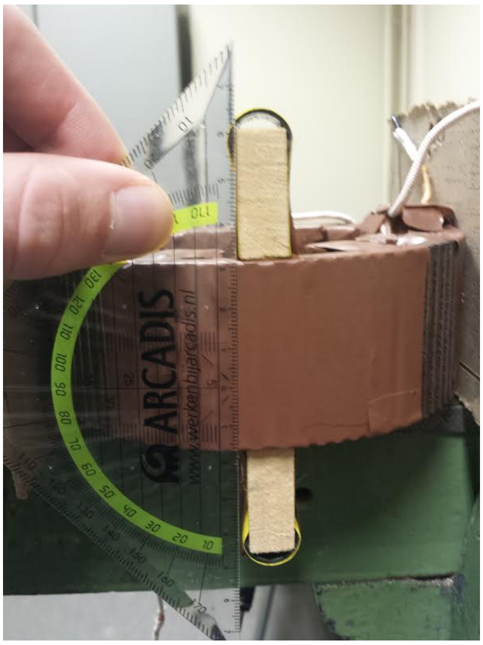

Figure 3.4: Spacers for coil 4

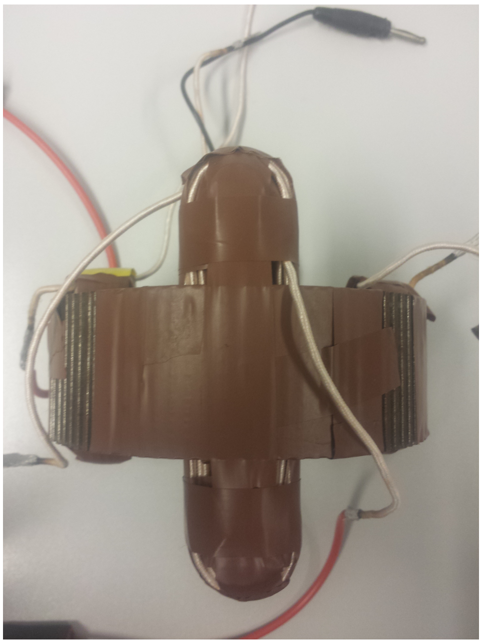

Figure 3.5: Coil 4 fixed with electrical tape

To neglect the skin effect and the proximity effect in the coils they are wound with Litz wire. For a sample piece of one meter of the used Litz wire, a nearly constant resistance for frequencies up to 10kHz is confirmed with an impedance analyser (Agilent 4294A). Details about the coils are given in Table 3.2. The end-winding height h, as shown in Figure 3.1, is measured with a digital ruler and the resistance is measured by applying a 4-wire measurement.

Table 3.2: Coil details

	Position	**Turns**	**End-winding height (mm)**	**Resistance ($m\Omega$)**
Coil 1	$0°$	18	0	20
Coil 2	$90°$	18	0	20.1
Coil 3	$180°$	18	34	40.3
Coil 4	$270°$	18	7	24.5

To measure the iron losses in the stator, one of the coils is connected to the power source. During the measurements, the stator is placed on a wooden table so no additional iron losses will be induced in objects other than the stator core.

3.1.2. Experimental procedure

The measurement system is automated so human errors are excluded as much as possible. A laptop with MatLab installed is controlling the input values (voltage and frequency) of a AIM TTI TG5011 function generator according to feedback from a Yokogawa DLM2034 Mixed signal oscilloscope, measured by a Yokogawa IM701933-01E current probe. The signal is amplified by a KEPCO BOP linear power amplifier that is set to constant voltage mode. The amplifier added a significant amount of dc offset during the initial measurements. Therefore, the output of the power amplifier is filtered by a passive filter so no DC current can pass. The filtered current is applied to the connected coil on the stator. Before each measurement step AC demagnetization is performed. After each successful measurement, it forces the amplitude of the magnetic field slowly to zero by decreasing the input voltage. This demagnetization process turned out to be necessary to remove the residue of the stored magnetic energy from the preceding measurement.

By applying a frequency sweep for predefined excitation currents, the exitation current waveform and the coil voltage waveform can be measured for different frequencies. The control algorithm controls the current to a given target current by adjusting the input voltage. It makes sure that the waveforms are only stored when the measured rms current is equal to the target current. In practice, this gave some difficulties and slowed down the process. A few degrees of freedom are added to overcome these difficulties. If the measured rms current is within the range $I_{target} \pm \delta$, the program is allowed to store the measured data and continue with the next frequency step. δ is the allowed error and is set to $0.5\% \cdot I_{target}$. The allowed error is small enough to assume that the measured rms current is the target current. This addition turned out to improve the measurement speed a lot without losing its accuracy.

The total loss P_t is obtained by averaging the instantaneous power calculated by multiplying the measured excitation current waveform and the coil voltage waveform. The coil resistances R are known, which means that the total iron loss induced by each coil can be calculated by

$$P_{iron} = P_{total} - P_{copper} = P_{total} - I_{rms}^2 R \tag{3.1}$$

3.2. Measurement results and discussion

Figure 3.6 shows the measured iron losses. The losses are plotted versus frequency and the RMS value of applied sinusoidal excitation current. The course of the measured iron losses is theoretically correct, i.e., exponential growth with current and frequency. Less iron loss P_t is measured in coil 3 (34 mm) when compared to coil 1 (0 mm). However, this is also true for coil 2 (0 mm), which should give approximately the same iron loss as coil 1 (0 mm). This will be further examined.

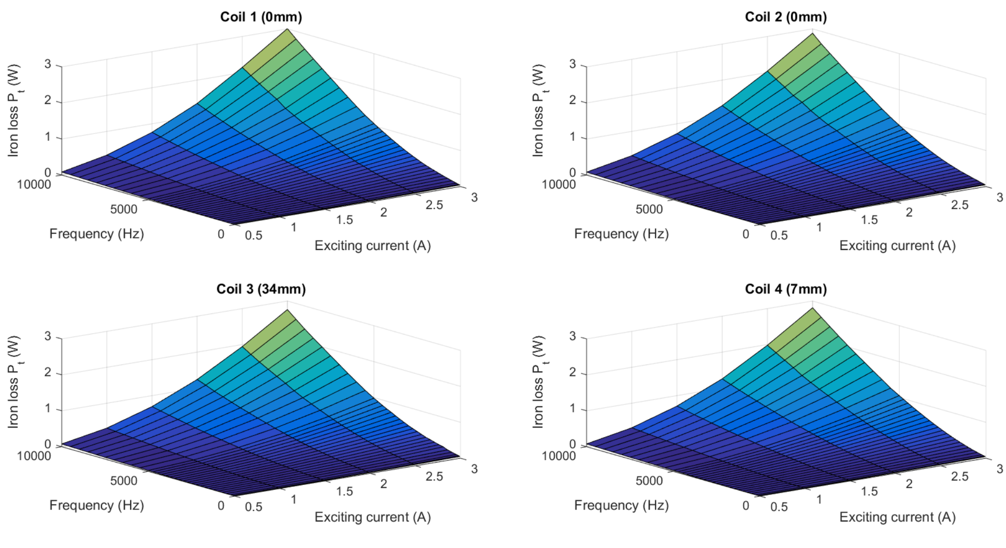

Figure 3.6: Measured core losses all coils

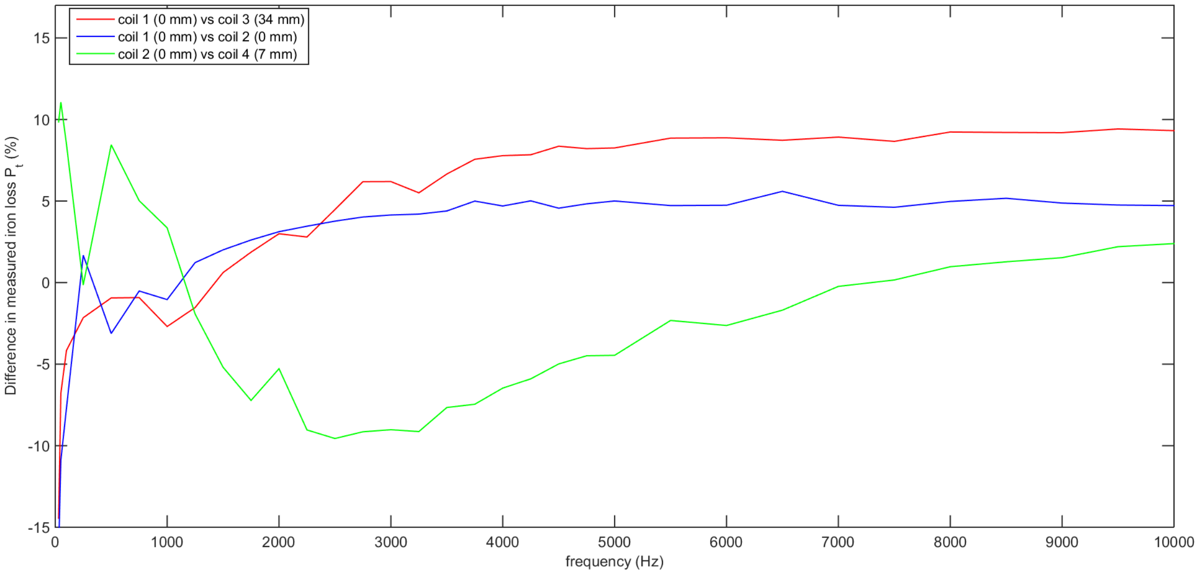

Figure 3.7: Difference in measured iron loss for different coils

The difference in measured iron loss versus the frequency is shown in Figure 3.7. The differences for each exiting current are averaged for the same frequencies. The variation in loss difference for low frequencies is not logical and can be explained as follows; the measured iron losses in the stator core are so small for frequencies up to 2 kHz, that a small measurement error can result in a misleading percentage error. For higher frequencies, i.e., higher iron losses, the iron loss difference converges to a nearly constant value. The losses induced by reference coil 1 (0 mm) are 8-9.5% higher than the losses induced by coil 3 (34 mm). This would imply a significant impact of high-frequency end-winding induced iron loss on the total iron loss in this stator core. However, it should be mentioned that there is also a difference of 5% between the measured iron loss from coil 1 (0 mm) and coil 2 (0 mm).

The only difference between coil 1 (0 mm) and coil 2 (0 mm) is the coil position. This suggests that the material properties in both stator teeth are different. It is known that soft magnetic material is degrading due to manufacturing process of laminated cores [55][56]. In addition, interlaminar faults, mainly due to deterioration of the electrical insulation, can influence the iron losses [57]. Theoretically, it is safe to conclude that the 5% difference in iron loss between coil 1 (0 mm) and coil 2 (0 mm) are due the non-homogeneous magnetic properties in the stator core. The effect on the magnetic properties of opposing teeth will probably be less as the rolling direction for those teeth is the same due to symmetry. This can be studied by putting identical coils on opposing teeth of the stator and compare measured iron losses. However, this is beyond the scope of this Thesis.

If 5% of the 8-9.5% difference in iron loss between coil 1 (0 mm) and coil 3 (34 mm) is due to the varying material properties, then still 3-4.5% can be accounted to end-winding induced iron losses. In addition, by elevating the end-winding height, the elevated 'straight' part of the end-winding still generate leakage fluxes that penetrate the laminations in laminar direction. It is not possible to separate the end-winding induced iron loss from the total iron loss P_t. However, the total iron losses can be altered a significant amount by varying the end-winding height. Therefore, the impact of end-winding induced iron losses on the total iron loss of the tested stator core is significant for frequencies above 2 kHz. Validity of this statement will be tested numerically in chapter 4.

The difference in iron loss P_t of coil 2 (0 mm) and coil 4 (7 mm) is harder to explain. Even for a small elevation of the end-winding, reduction in the measured iron loss is expected. However, multiple measurements gave the loss difference shown in Figure 3.7. For frequencies between 1 kHz and 7 kHz, the losses induced by coil 4 (7 mm) are larger than those by coil 2 (0 mm). This can have several reasons.

1. The measured difference in losses can be accounted to varying material properties in stator core.

2. The inductance changes with the end-winding shape, influencing the created magnetic flux [58].

3. One of the coils can have bad connection to the power source. The ends of the coils are tinned in a tin bath to melt the insulation of each copper strand and connect all the internal strands of the Litz wire. If this is not done properly, wrong results can be achieved.

Varying material properties are already discusses and will have some influence on the induced iron loss. A fault in the tinning process is not likely as the measured resistance for coil 4 is larger than coil 2, as expected, because the wire length is slightly longer. However, the calculated self-inductance is less, as shown in Figure 3.8. This is make sense as it is known that the greater the magnetic permeability of the core which the coil is wrapped around, the greater the inductance. The end-winding of coil 2 has a higher inductance than the end-winding of coil 4, which is mainly influenced by air. It is also known that the inductance increases with increasing coil area, this explains the higher inductance of coil 3.

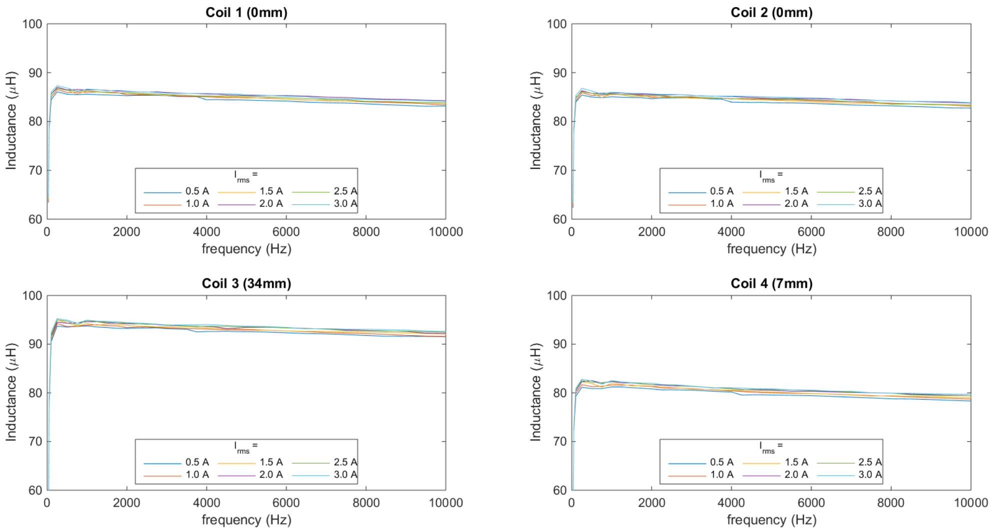

Figure 3.8: Coil inductances versus frequency

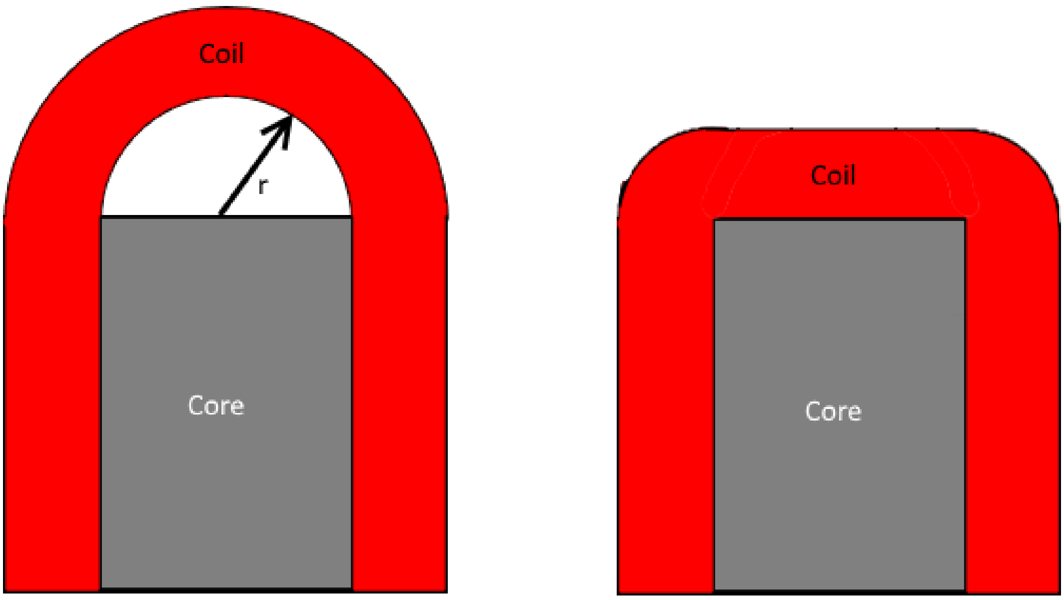

Figure 3.9: End-winding shape coil 4 (left) and coil 2 (right)

The magnetic flux can also be altered by the end-winding shape. Figure 3.1 shows the end-winding shapes for coil 4 (7 mm) and coil 2 (0 mm). The magnetic field due to a current element is described by the Biot-Savart law. If the current element is a wire (w), like in coil 2, the magnetic field at a distance a from the wire is given as

$$B_w = \frac{\mu_0 I}{2\pi a} \tag{3.2}$$

If the current element is a semicircle (sc) with radius r, like in coil 4, the magnetic field in the center is given as

$$B_{sc} = \frac{\mu_0 I}{4r} \tag{3.3}$$

The ratio between B_{sc} and B_w is given as

$$\frac{B_{sc}}{B_w} = \frac{\pi a}{2r} \tag{3.4}$$

The ratio of a with respect to r is around 1/7 in the experiment. According to the Biot-Savart law, a weaker field and less losses near the end-lamination are expected for coil 4, contradicting the measurment results. The only theories that seems to support the fact that coil 4 induces more losses than coil 2 is varying material properties or a measurement error.

3.3. Chapter conclusion

The aim of this chapter was to build an experimental setup to measure the impact of end-winding induced iron loss on the total core loss in a laminated stator core. Varying end-winding heights are used to show this impact. The following conclusions can be made:

1. It is not possible to differentiate the effect of hysteresis loss, eddy-current loss and excess loss.
2. Iron losses are evidently altered by the non-homogeneous material properties of the laminated core.
3. A coil with approximately the same resistance, inductance and end-winding shape can generate different losses in another stator tooth.
4. Iron losses in the tested stator core can be altered significantly by changing the end-winding.
5. The iron loss measured for a coil with an extremely elevated winding induces up to 10% less iron losses in comparison with a coil with an end-winding close to the stator core.
6. The iron losses are increasing exponential for higher excitation frequencies.

It is not possible to tell what the exact impact of the impact of end-winding induced iron loss on the total core loss in a laminated stator core is. However, it can be concluded that the iron losses can be influenced significantly by changing the end-winding shape.

4

Finite element method

Chapter 4 aims to

- Develop a 3D model with a commercial FEM package to study end-winding induced iron losses .
- Simulate the possible effects of electrical frequencies on end-winding induced eddy-current losses.

Section 4.1 starts with a brief introduction to the finite element method and the used commercial FEM package. The simplified 3D model to analyse high-frequency end-winding induced iron loss is described in section 4.2. Next, in section 4.4, the results of the finite element analysis are shown and discussed. In section 4.5 a 3D stator model is proposed for further research. Finally, conclusions drawn from the finite element analysis are given in section 4.6.

4.1. Introduction to the finite element method

The finite element method is an attractive way to estimate iron losses in electrical machines. Usually, a cross-section parallel with the laminates of the iron core is discretized into a mesh grid consisting of finite elements. The 2D field solution is used in the post-processing stage to calculate the iron losses by applying 1D iron loss equations discussed in section 2.2. A more elegant approach is to model the eddy-current losses and take into account the hysteresis and excess losses by incorporating a dynamic hysteresis model in the time-stepping scheme. However, this is not yet a common practice [25].

The focus of this chapter is on modelling the eddy-current losses as those are dominant at high frequencies. Eddy currents in the laminations in such a 2D model are wittingly ignored. This is mainly due to the fact that 3D models are very extensive for most computers. To study end-winding the impact of end-winding induced eddy-current without neglecting the the main magnetic field, the laminations must be modelled explicitly in a 3D model. A powerful computer is available.

The commercial FEM package COMSOL Multiphysics® software is used to perform the modelling [59]. The software provides the AC/DC module for simulating electric, magnetic, and electromagnetic fields in static and low-frequency applications. The frequencies in electrical machines are classified as 'low'. The following sequence is used in the FEA.

1. Build the simplified 3D model where each lamination is defined explicitly.
2. Apply the appropriate physics and boundary conditions to the problem.
3. Discretize the model with a mesh that is fine enough to retrieve the skin depth at the lamination boundaries.
4. Simulate the 3D model.
5. Analyse the results in the post-processing stage.

4.2. Model description

A simplified 3D model to study the impact of end-winding induced eddy-currents is proposed. Figure 4.1 shows the model for the finite element analysis. It consist of a concentrated winding around a rectangle core sample with 39 steel sheet laminations with a thickness of 0.5 mm. To reduce the computing time, the analysed region is reduced to 1/8 of the model. The material properties of the objects are given in Table 4.1. The conductivity is taken from the stator core used in chapter 3. A rather low constant relative permeability is chosen to make sure the magnetic flux density in the core will stay within acceptable limits.

Table 4.1: Material properties of the objects in the FEM model.

Object	Material	Rel. permeability	Conductivity (S/m)
Winding	Copper	1	5.998e7
Core	Iron	1000	2e6
Insulation	Air	1	0
Surroundings	Air	1	0

Proper boundary conditions are selected at the symmetry boundaries to ensure continuity of the current and the magnetic field. To model the coil insulation and the insulation between the laminations, a magnetic continuity boundary is chosen with perfect electrical insulation properties, so no current can cross. A normal current density boundary is applied to one side of the coil. To make the current flow, a ground boundary is used at the other. In addition, the Ampère's law and current conservation node is applied to all laminations to guarantee that the sum of the eddy-currents in each lamination is zero.

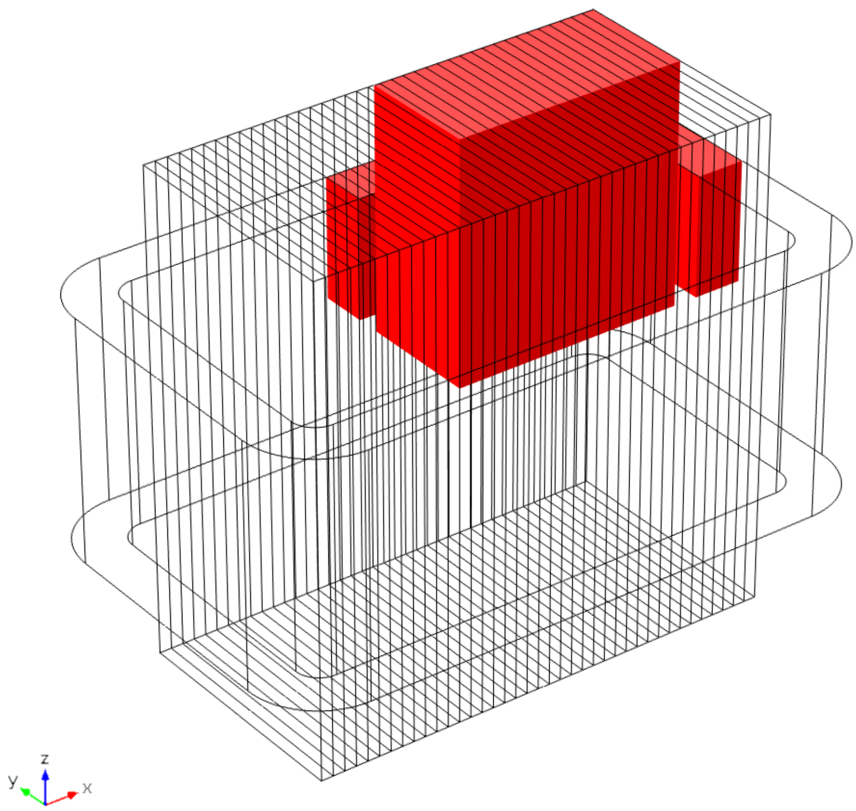

Figure 4.1: Simplified 3D model where the analysed region is highlighted in red

The dimensions of the mesh elements near the lamination boundaries are determined considering the theoretical skin depth. At high excitation frequencies the skin depth will become smaller than the lamination thickness. As explained before, the skin depth is the length of penetration over which the magnitude of the field decays to $1/e$. A high gradient of the magnetic field is expected in this skin depth area. This means that the model needs to be discretized in such a way that the correct magnetic field gradient can be retrieved. The theoretical skin depth at several frequencies for the analysed core material, calculated by equation 2.8, is given in Figure 4.2. Above 500 Hz the skin depth becomes smaller than the lamination thickness, introducing the skin effect.

Ideally, the model should be remeshed every frequency iteration so that a minimum of two elements are present in the skin depth length. However, the model is so large that this will take to much simulation

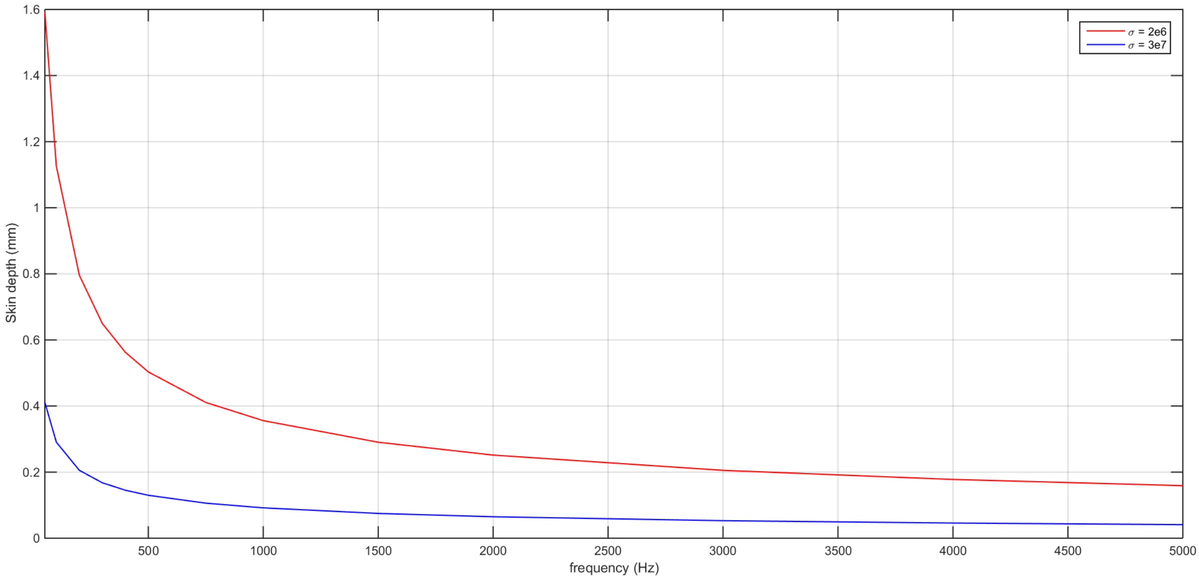

Figure 4.2: Theoretical skin depth versus Frequency for the specified core material

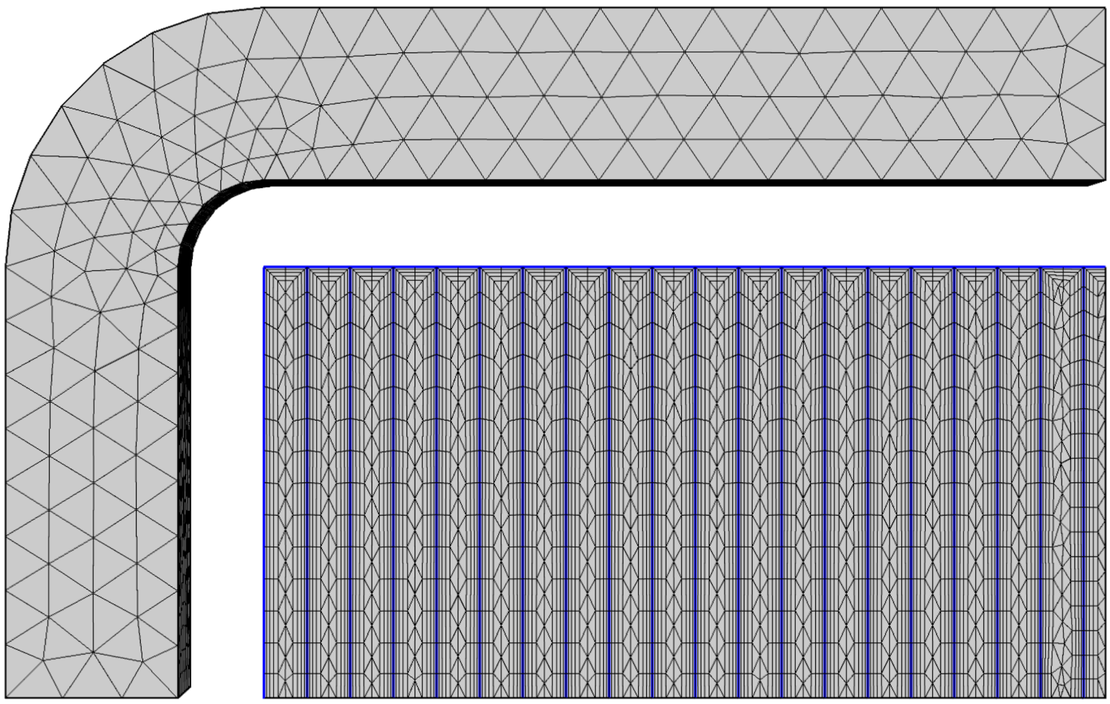

Figure 4.3: XY-view of the discretized finite element model

time. Instead, the skin depth δ at 1000 Hz, $\delta(1000)$, is chosen to define the boundary layers of the mesh that will be used for all frequencies. It turned out that this value is good enough for this problem. As shown in Figure 4.3, three boundary layers are defined inside the laminations. The width of each boundary layer is $1.2^{n-1} \cdot \delta(1000)/3$, where n is the nth boundary layer.

A current density of 6e7 A/m^2, varying with the frequency of interest, is applied to the normal current density boundary in all simulations. The winding is modelled as a solid copper bar, while this is normally a strand of copper wires. It is not possible to model such a winding with the Magnetic and Electric Field (mef) environment within COMSOL. This means that the copper bar will be subject of the skin effect, changing the inductance of the winding, and with that, the induced magnetic field at higher frequencies. This will not be a problem in the study to end-winding induced eddy-current losses if only the values measured at the same frequencies will be compared.

The dimensions of the analysed core region are 5 × 10 × 9.5 mm. The coil width is 2 mm and the coil height is 5 mm, which is half the original coil height. The distance between the coil and the core is chosen to be 1 mm. If this distance was 0 mm, the coil and the core would share boundaries at every lamination, influencing the mesh quality in a negative way.

Two additional models are created; one with no end-winding and one with an extended end-winding. The results of these models will be compared to the model introduced in this chapter. The modified model with no end-windings is shown in Figure B.1. The modified model with an extended end-winding is given in Figure B.2.

4.3. Model assumptions

The following assumptions are made in the simplified 3D model:

- The hysteresis losses and excess losses are neglected in all models.
- The magnetic flux path is not able to close through the core and is forced to close through air as the core sample has finite lengths in the main flux direction. Additional losses will be introduced at the core ends. This model can be seen as a stator tooth with two ends. Usually, one end of the tooth is connected to the a yoke that connects all the other stator teeth.
- The lamination material is assumed to be isotropic, i.e., the material has identical values of a property in all directions. In reality this is not true for most laminated steel sheet.
- The laminated core is assumed to have linear magnetic properties. However, in reality, the steel sheet laminations are ferromagnetic and has non-linear magnetic properties with a varying magnetic permeability. See Appendix A for an introduction to ferromagnetic materials.
- For simplicity, the insulation is modelled as perfect electric air insulation with zero thickness. In reality, the insulation consists of a combination of air and coating. It has his own thickness and reduces the effective area of the core.
- The coil is modelled as a copper bar, where in a real electrical machine the coil consists of a strand of copper wires. This is already discussed in the model description section.
- The excitation current is assumed to be perfectly sinusoidal. However, in real applications the electrical machines is fed by a frequency converter, which produces excitation waves with higher space harmonics.
- The coil is chosen to have a racetrack shape where the end-winding is parallel with the lamination direction. In electrical machines, the coil can have different end-winding shapes, which create different magnetic fields in the end-winding region.

4.4. FEA results and discussion

The results are presented in this section. First, the modelled magnetic flux and current density distribution are given in subsection 4.4.1. Subsection 4.4.2 dives deeper into the eddy-current losses simulated with the 3D FEM model. Finally, in subsection 4.4.3, the results will be compared to the solution of a model with an elevated winding to validate the experimental results found in Chapter 3.

4.4.1. Magnetic flux and current density distribution

Figure 4.4 shows the flux density distribution in the simplified model. The results of the model with a high-conductivity core are presented in Appendix C. The flux is non-uniformly distributed in the top laminations of the stack. The magnetic field concentrates mainly under the coil and near the edges of the end-laminations. Near the core ends a void space emerges where the magnetic field is pushed to the lamination edges. The flux densities in the end-lamination are also significantly higher than in the middle of the stack. For higher frequencies the flux density increases in the whole core, especially in the top laminations near the end-winding.

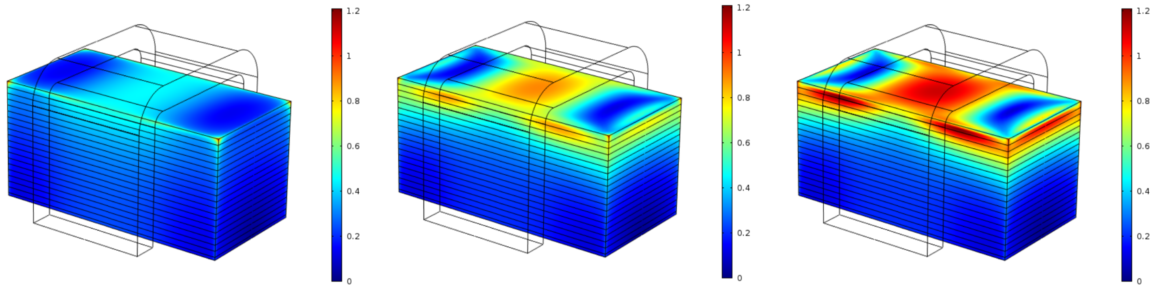

Figure 4.4: Magnetic flux density (T) distribution for 50 Hz (left), 500 Hz (middle) and 1 kHz (right)

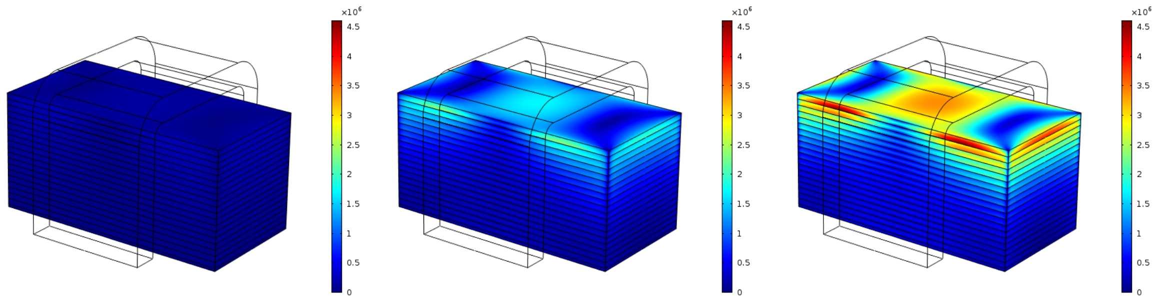

Figure 4.5: Induced current density (A/m^2) distribution for 50 Hz (left), 500 Hz (middle) and 1 kHz (right)

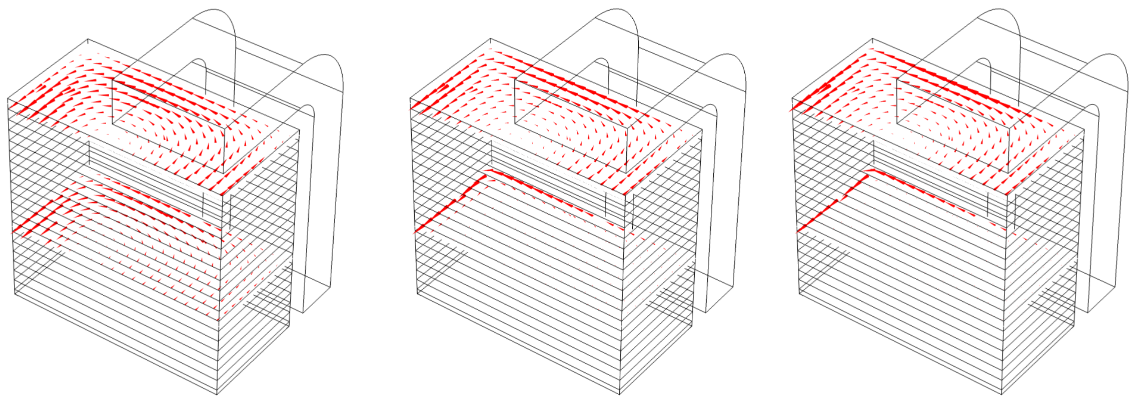

Figure 4.6: Eddy-current path for 50 Hz (left), 500 Hz (middle) and 1 kHz (right)

The 3D eddy-current distribution is shown in Figure 4.5. The eddy-current are distributed like the magnetic flux density. The eddy-currents with the strongest magnitude are in the top laminations near the end-winding. When the skin-effect emerges, in this case for 1000 Hz, the induced current density increases significantly. Figure 4.6 shows the eddy-current path in the middle of the top lamination and in the middle of a center lamination. The magnitude of the arrows in both planes can not be compared as they are enlarged for clarity. The in-plane eddy-current can clearly be seen in the top lamination. The eddy-currents close through the core ends, as in this model there is no other path to go. The decaying component of the in-plane eddy-currents is studied further in 1D.

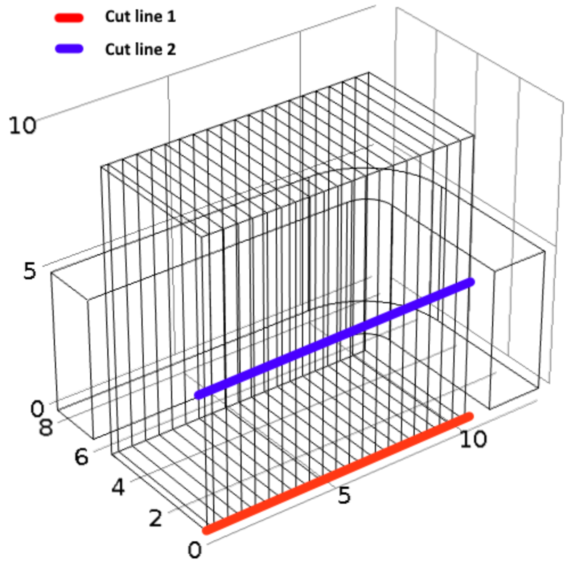

Figure 4.7: Cut lines to study flux and current density inside the laminations

Figure 4.7 shows two cut lines. The flux and current distribution inside the laminations are studied using those cut lines. Figure 4.8 and Figure 4.9 shows the flux and current density inside the laminations along cut line 1, respectively. Figure 4.10 and Figure 4.11 shows the flux and current density inside the laminations along cut line 2, respectively. For frequencies below 500 Hz the magnetic flux is going through the laminated stack with a minor change due to the counter magnetic fields created by the eddy currents. The skin effect emerges clearly for frequencies above 500 Hz. The magnetic flux density is higher near the end-winding disregarding the applied frequencies. As the frequency increases, the skin effect emerges, such that the current density is largest near the surface of the conductor. The current density decays toward the middle of the lamination. For the middle of the stack, the large currents near the surface creates a large counter magnetic field that pushes to main field from the middle of the laminations to the surface. For the end of the stack, due to the decaying in-plane eddy-currents component, the surface currents at the end-winding side are larger than at the other side of the lamination. This will push the magnetic field outside the middle, away from the end-winding, as shown graphically in the cut line figures. It is also noticed that the eddy-currents under the end-winding (cut line 1) penetrate the laminations much deeper than at the end of the coil (cut line 2).

Appendix C shows the results for a stator with a conductivity of $3e7\ S/m$. This is a highly unlikely case in electrical machinery. However, it shows that the induced magnetic field and current density are significantly higher for a material with a higher conductivity. If the value is altered in the manufacturing process of the stator, it can really influence the eddy-current losses.

In summary, the magnetic flux and current density near the end-winding

- are non-uniformly distributed over the laminations in all directions.
- are influenced by the skin effect at higher excitation frequencies.
- do have an in-plane component decaying towards the center of the stack.

These finding are already described in literature, and hereby confirmed numerically. There will be no simple way to develop an analytical model for the current density distribution in end region of the core. It is probably better to put more effort in improving and extending the homogeneous modelling techniques discussed in Chapter 2.

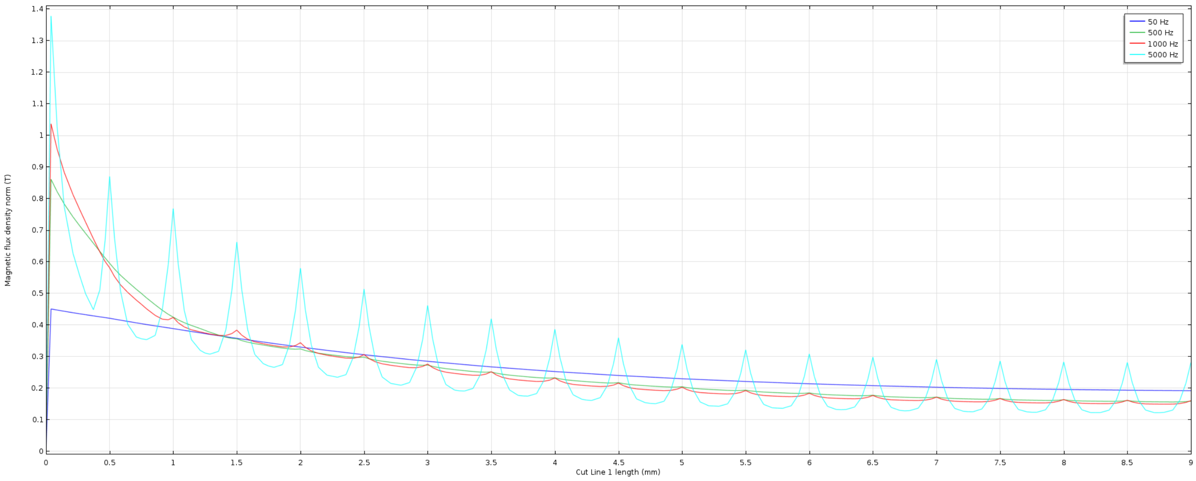

Figure 4.8: Magnetic flux density along cut line 1

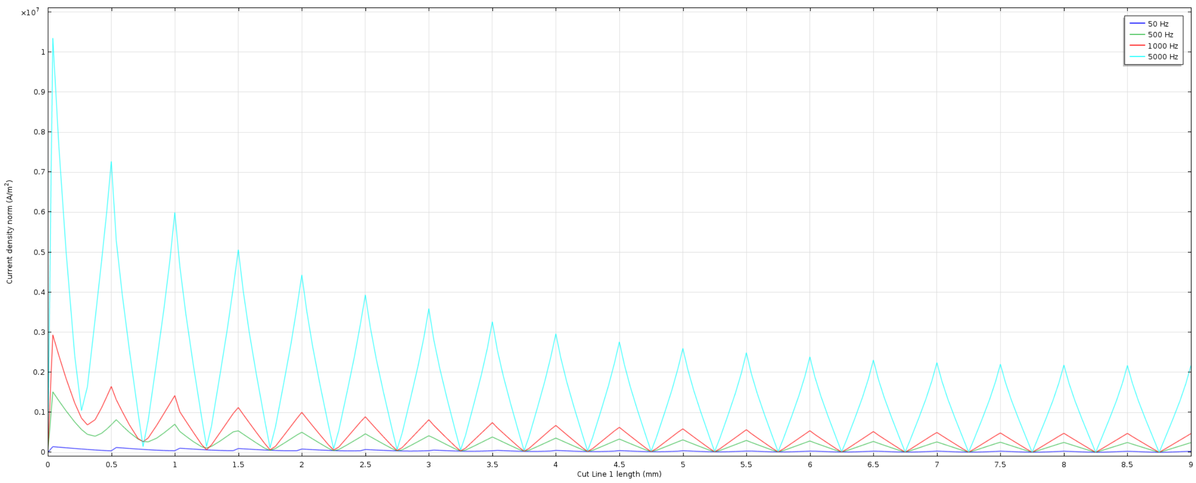

Figure 4.9: Current density along cut line 1

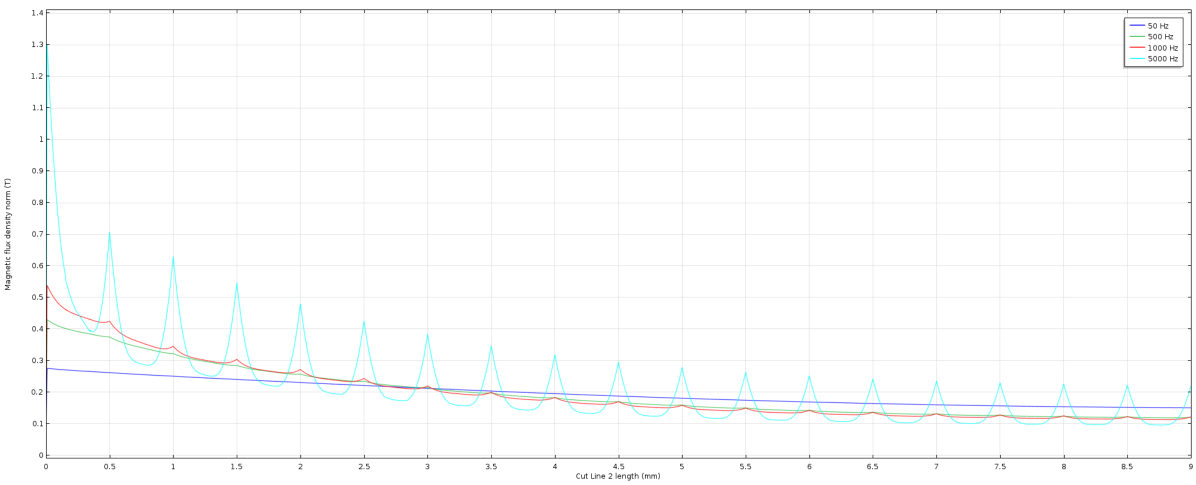

Figure 4.10: Magnetic flux density along cut line 2

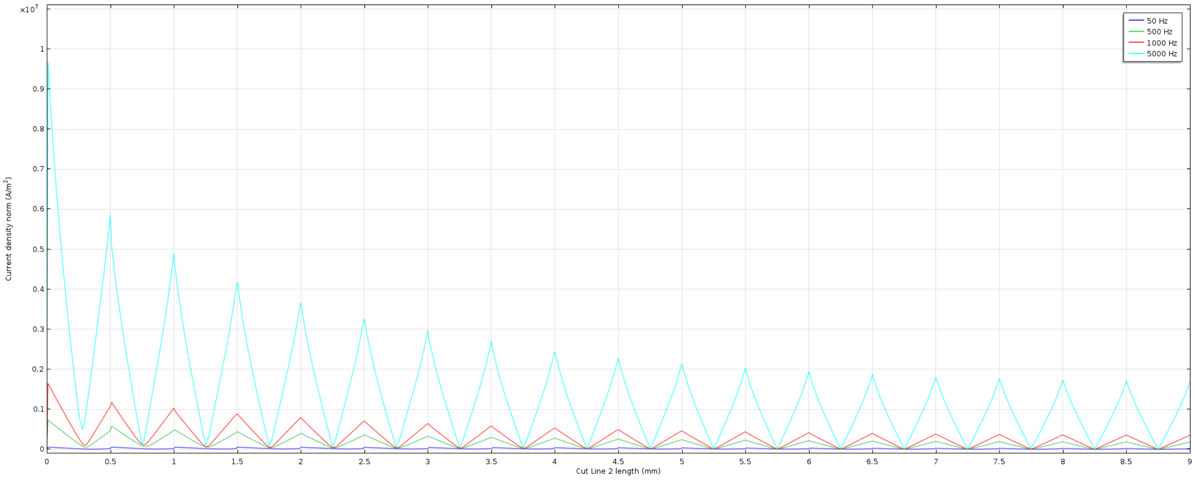

Figure 4.11: Current density allong cut line 2

4.4.2. Eddy-current losses

The eddy-current losses in the modelled sample are evaluated for several excitation frequencies. Figure 4.12 shows the eddy-current loss versus frequency for the model with end-winding, without end-winding and the extended end-winding. As expected, the losses increase exponentially with time. As show in Table 4.2, the losses in the model with the end-winding are up to 3355 % higher than the losses in the model without an end-winding. This implies loss correction factors that needs to be used from 7 up to 30. A large amount of those extra losses can be accounted to the additional losses in the core ends where the eddy-current is forced to turn around. However, this will also happen in the teeth tips of the stator as will be shown in section 4.5.

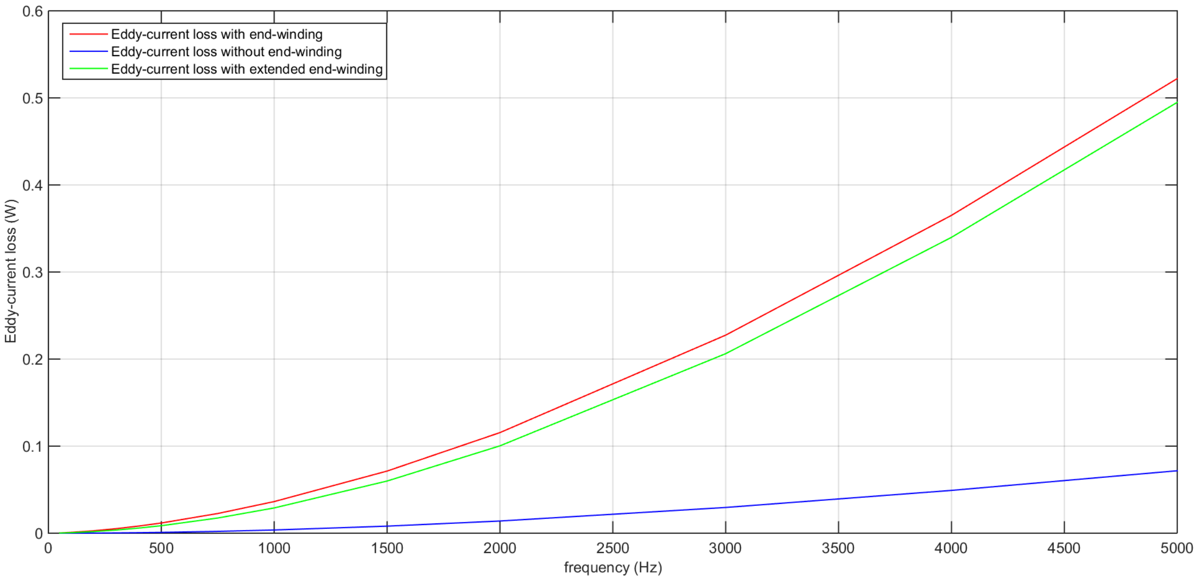

Figure 4.12: Eddy-current losses in the core sample

Figure 4.13 shows the eddy-current loss inside each lamination as percentage of the total iron loss in the modelled iron core with an end-winding. For all frequencies, 80% of the eddy-current losses in the studied iron stack are induced in top six to eight laminations. In addition, the eddy-currents increase quadratically with frequency. This means that for high frequencies enormous losses, i.e, rise in temperature, are introduced in the top laminations near the end-winding, with emphasis to 'near'. It should be noted that the results are for the part of the core that is encapsulated by the winding, usually the stator tooth. For core parts at a distance of the coil, i.e., in the yoke, the magnetic flux and the losses will be uniformly distributed over the laminations, provided that skin effect and edge effect

Table 4.2: Modelled eddy-current losses; with end-winding (EW) versus without end-winding (noEW)

Frequency (Hz)	$\mathbf{P_{EW}}$ (W)	$\mathbf{P_{noEW}}$ (W)	**Difference (%)**
50	0.00033	0.00001	3355
100	0.00069	0.00004	2431
200	0.00278	0.00015	1733
300	0.00521	0.00034	1431
400	0.00820	0.00060	1258
500	0.01170	0.00094	1144
750	0.02261	0.00210	977
1000	0.03633	0.00370	883
1500	0.07137	0.00810	781
2000	0.11555	0.01399	726
3000	0.22752	0.02956	670
4000	0.36509	0.04916	643
5000	0.52218	0.07173	628

can be neglected. In addition, it is kept in mind that the values shown in Figure 4.13 are relative. For electrical machines with longer axial length, the losses in the end-laminations will be a smaller part of the total eddy-current loss. However, in the introduction of this Thesis it is said that high speed electrical machines show the trend of decreasing axial lengths. It can be concluded that the impact of end-winding induced eddy-current losses on the total iron loss will become more significant with decreasing axial lengths of the iron core.

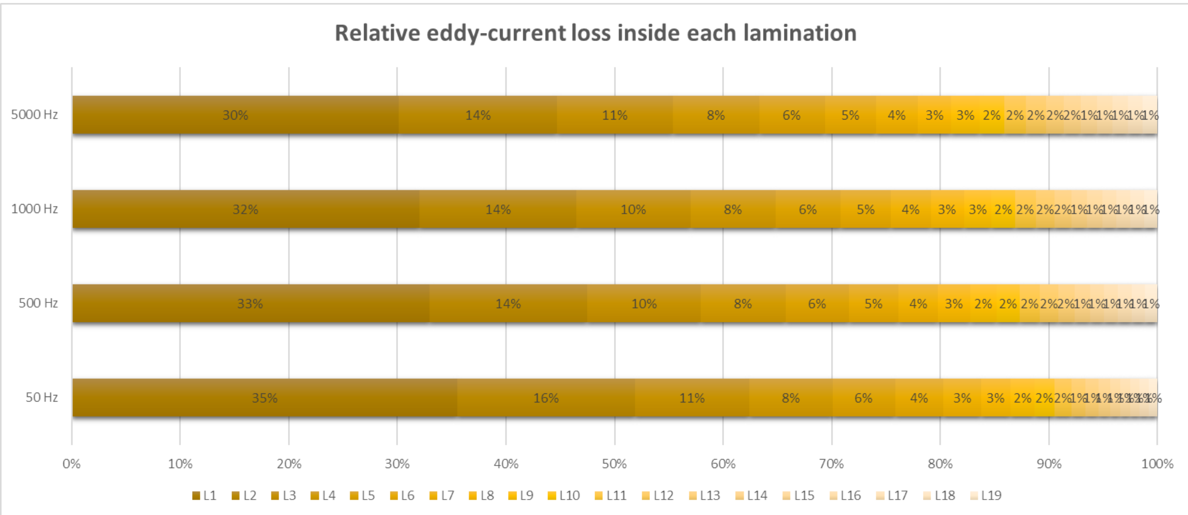

Figure 4.13: Relative eddy-current loss inside each lamination: L1 (top lamination)

The validity of the 1D eddy-current loss model given in equation 2.6 is tested against the numerical results. For clarity, the equation is repeated in equation 4.1.

$$P_e = \left(\frac{\sigma\pi^2 d^2 f^2 \hat{B}^2}{6}\right)\left(\frac{3(\sinh\gamma - \sin\gamma)}{\gamma(\cosh\gamma - \cos\gamma)}\right)\Delta V \tag{4.1}$$

where ΔV is the volume of the analysed core. All parameters, except the magnetic flux density, are directly available from the model description given in section 4.2. The magnetic flux is calculated normal to an integration surface s by

$$\Phi = \int_s \nabla \times \mathbf{A} \cdot \mathbf{n} ds \tag{4.2}$$

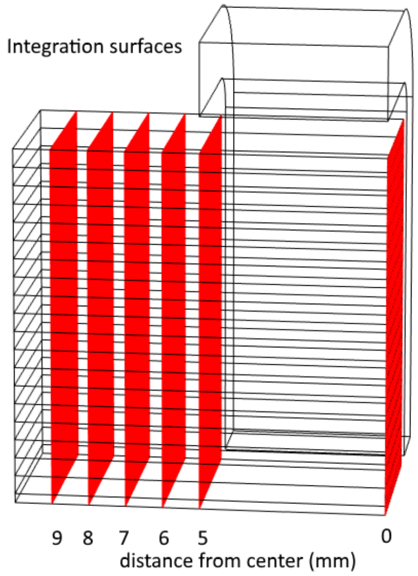

Figure 4.14: Integration surfaces to calculate B

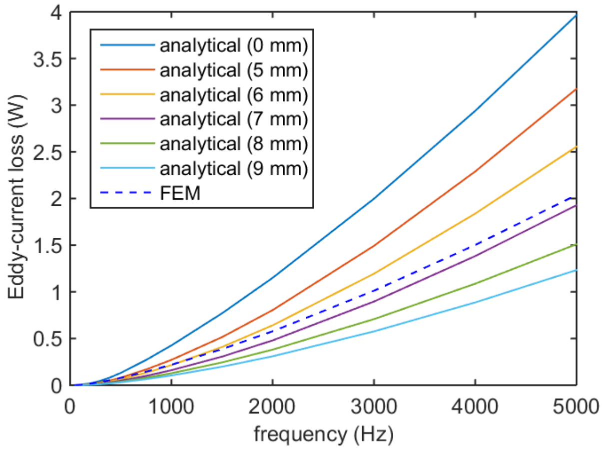

Figure 4.15: Eddy-current loss versus frequency

where $\mathbf{A}$ is the magnetic vector potential. The magnetic flux density is achieved by dividing the calculated flux by the surface area. Usually, the integration surface is placed normal to the main flux in a part of the iron core where the flux is not altered by, for example, the end-windings. Unfortunately, this is not possible in this model, so the integration surfaces are placed near the end-winding. Figure 4.14 shows the integration surfaces to calculate the flux density for the traditional analytical 1D model. The results are given in Figure 4.15.

The magnetic flux decreases as the distance to the coil increases. Evidently, the effect of the end-winding induced eddy-currents on the main magnetic flux declines. Equation 4.1 underestimates the eddy-current losses if the flux is evaluated on the integration surfaces near the coil. It overestimates the losses when the flux is evaluated on the surfaces at some distance from the coil. It is noticed that the fluxes are not yet stabilized, as they are still influenced by the end-winding at the end of the core. However, this means that in the stabilized region, where the flux normally is achieved, the flux will be even lower, i.e., equation 4.1 will underestimate the total eddy-current loss near the end-winding significantly.

4.4.3. Numerical validation of the experimental results

The model with extended end-windings is also numerically solved. The end-winding is extended to a distance of 8 mm to the iron core. Figure 4.16 shows the eddy-current losses from the original end-winding model and from the extended end-winding model. The difference between the two models is

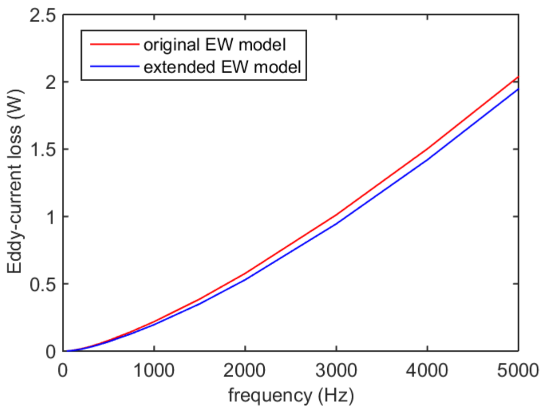

Figure 4.16: Modelled eddy-current loss versus frequency

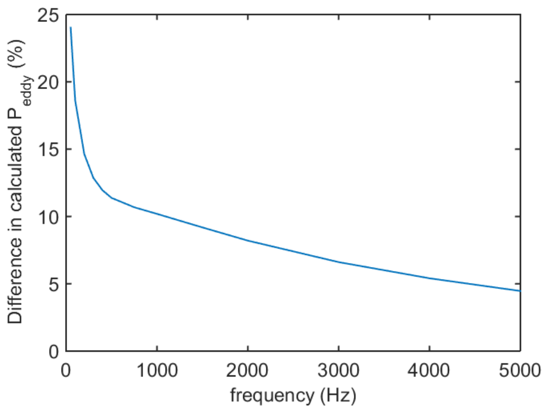

Figure 4.17: Difference in eddy-current loss versus frequency

shown in Figure 4.17. More eddy-currents are introduced in the normal situation, which is in agreement with the experimental results from Chapter 3. It is noticed that the models are completely different than the stator core used in the experiment. However, by applying the same theory, i.e., increasing end-winding height results in descreasing losses, it is shown that the total losses can be influenced significantly.

4.5. Future work: A laminated stator model in 3D

The modelling technique that is used in this chapter can also be used to a stator core. The analysed region consists of ten laminations (d = 0.35 mm) and converged to a solution for 50, 100 and 200 Hz. Figure 4.18 and Figure 4.19 are showing the magnetic flux distribution and the current density for

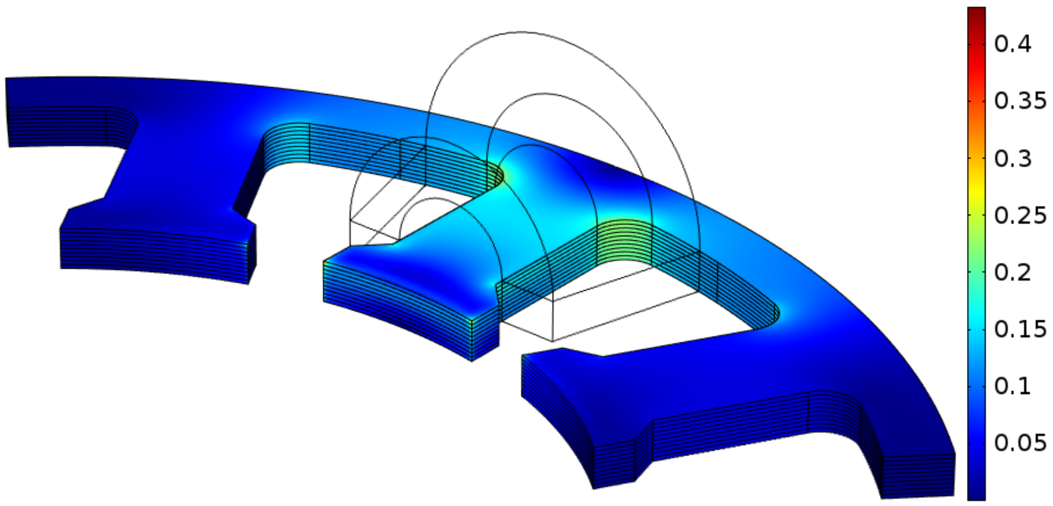

Figure 4.18: Magnetic flux density (T) distribution in a stator core sample for f=200 Hz

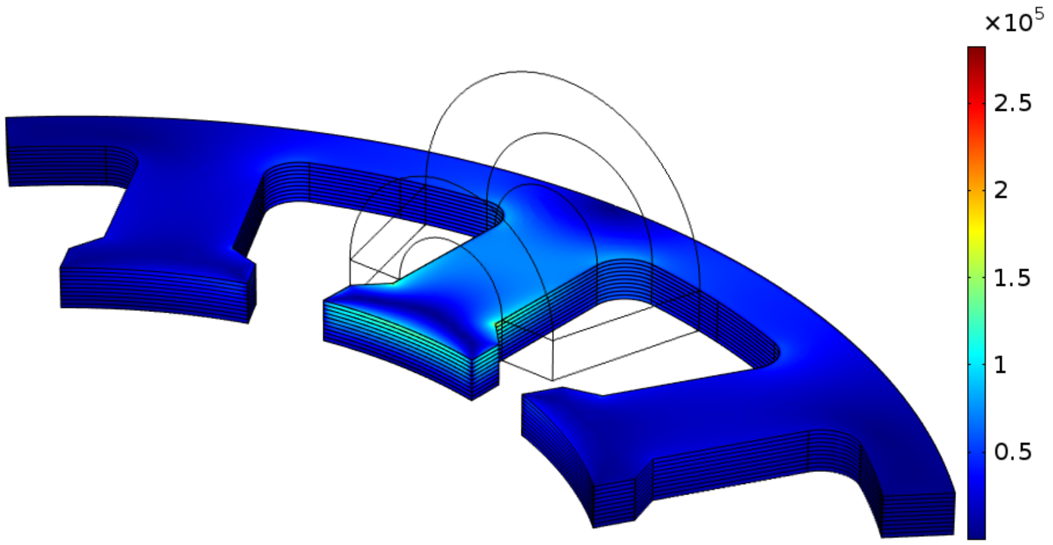

Figure 4.19: Induced current density (A/m^2) distribution in a stator core sample for f = 200 Hz

200 Hz, respectively. The conductivity of the material is chosen to be 2e6 A/m^2. The skin effect in the lamination direction due to the main magnetic field can be neglected.

It has to be mentioned that the model is not perfect. The mesh has to be refined. Only one triangular mesh layer along the lamination thickness of each lamination is used. This should be a minimum of two for frequencies where the skin effect can be neglected. Three to four mesh layers should be used in the top layers as the magnetic field is pushed to the bottom of the lamination as is shown in the simplified 3D model earlier in this chapter. The used computer was not powerful enough to solve for the described mesh. However, the showed result is a good approximation of how the magnetic flux and eddy-currents are distributed. In future research this model has to be improved.

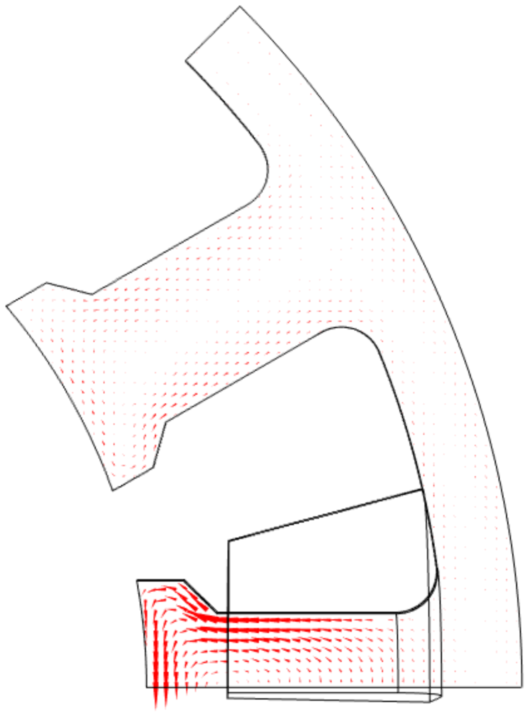

Figure 4.20: Eddy-current path in the center of the top lamination of the stator core

The magnetic flux and current density near the stator tooth tip is distributed in the same way as in the simplified 3D model. Figure 4.20 shows the eddy-current path in the center of the top lamination of the stator core. The eddy-currents collect at the lamination edges and the induced fields will push away the main magnetic field, creating a void in the middle of the tooth tip. Directly under the end-winding eddy-currents are more uniformly distributed and has a decaying component to the middle of the core. In the yoke, the flux propagate to the other teeth, where the distribution is the same as in the tooth which is encapsulated by the coil, only less in magnitude. The in-plane eddy-currents spread evidently through the entire core. The majority of the eddy-current losses in the analysed model are induced in the stator teeth, mainly due to the end-windings. The total volume of the teeth with respect to the volume of the core is increasing in high-speed electrical machines. This results in an increasing impact of the end-winding induced eddy-current on the total core loss.

4.6. Chapter conclusion

The aim of this chapter was to develop a 3D model with a commercial FEM package and to study the effect of high-frequency end-winding induced eddy-current loss with respect to the total loss numerically. In order to achieve this, a simplified 3D model is presented. The main conclusions from this model are as follows

1. The main magnetic field, the end-winding induced magnetic field and the counter magnetic field

induced by the eddy-currents are clearly influencing each other, and cannot be analysed separately in the end-winding region.

2. With the axial length getting shorter in HSEMs, up to 60-80% of the eddy-current losses near the coil are induced in the top six laminations at both sides of the iron stack.
3. In addition to the previous conclusion; Increasing excitation frequencies will results in significant eddy-current losses near the end-winding.
4. The traditional 1D eddy-current model underestimates the eddy-current losses near the coil significantly for fluxes chosen at a distance of the coil, especially for increasing frequencies.
5. Increasing the end-winding length reduces the total eddy-current loss in the core. This corresponds with the experimental results.
6. For frequencies where skin effect emerges, large currents are introduced at the lamination surfaces. Those currents have a decaying component moving inwards into the stator.

It is still not possible to tell exactly what the impact of end-winding induced iron losses on the total losses is. However, focussing on the core part near the coil, it is shown that a majority of the eddy-current losses are induced in the top laminations. It can be concluded that if the iron volume encapsulated by concentrated windings is relatively large to the total iron volume, the end-winding induced eddy-current losses cannot be neglected.

5

Conclusion and recommendations

The aim of this Thesis was to find a solution to the following research question:

What is the impact of end-winding induced iron losses on the total core losses in high-speed electrical machines with concentrated windings?

Several iron loss methods to estimate high-frequency iron losses provided by existing literature were discussed. The focus moved to eddy currents as it is expected to be the dominant part of high-frequency iron losses. Several 1D, 2D and 3D approaches were treated to analyse eddy-current in laminated iron. However, it was concluded that no provided method, except a brute-force 3D FEM model, is sufficient enough to estimate the real eddy-current loss distribution near the end-winding. The experimental results showed that the iron losses in the used stator are sensitive to changes in the end-winding shape, excitation current and frequency. In addition, two identical coils wrapped around distinct tooth induces different iron losses, which implies non-homogeneous material properties throughout the used stator. Extending the end-winding height resulted in a decrease in the total iron loss worth mentioning. This is also confirmed for the total eddy-current loss in the simplified 3D FEM model.

For high frequencies, where the skin depth is smaller than the lamination thickness, large eddy-currents are induced at the surface of the laminations. Due to the skin effect, the magnetic flux is pushed outside center of the laminations, reducing the effective flux carying area of the core. Independently of the skin effect, this also happens at core ends, for example, the end of a stator tooth. The in-plane eddy-current density is highest in magnitude near the end-winding and shows a decaying component to the middle of the stack. It is found that for 39 laminations with a thickness of 0.5 mm, 60-80% of the total iron losses near the concentrated coil are induced in the top six laminations at both core ends. In addition, the traditional 1D eddy-current model underestimates the iron losses near the coil significantly as the inserted magnetic flux amplitude is too low. The peak magnetic flux density for this 1D model is usually obtained at a distance from the coil in 3D models, or even worse, from 2D models, where the end-effects are neglected.

Back to the research question. For the used model, it is found that the impact of high-frequency end-winding induced eddy-current loss on the total core losses is serious in the core volume enclosed by the concentrated winding. Increasing machine speeds often imply shorter axial lengths as is visualised by the stator core used in the experiment. In addition, the volume of the core enclosed by concentrated windings becomes substantial with respect to the total core volume. The impact of high-frequency end-winding induced iron losses on the total core loss cannot be neglected in iron loss estimation of short axial high-speed electrical machines with concentrated windings.

5.1. Recommendations

The study focusses mainly on end-winding induced eddy current losses. However, iron losses also consist of hysteresis and excess loss. It would be interesting to look at the effect of the end-winding on those losses. In addition it is suspected the magnitude of the end-winding induced iron losses is dependent on geometry of the core, the end-winding shape, material properties of the steel and thickness of the laminations. Those are all interesting topics for further research.

The presented simplified 3D model is very extensive. The model had to solve over five million degrees of freedom. A simplified method to estimate the total iron loss, including the end-winding induced iron loss, should be developed. The discussed homogenization method looks promising and is a good starting point for this new method. However, the writer thinks that it is probably necessary to model the top laminations near core ends and end-windings explicitly.

Bibliography

[1] L. Silong, L. Yingjie, C. Wooyoung, and B. Sarlioglu, *High speed electric machines; challenges and design considerations,* in *Electrical Machines (ICEM), 2014 International Conference* (2014) pp. 2549–2555.

[2] N. Bianchi, S. Bolognani, and F. Luise, *Potentials and limits of high speed pm motors,* in *Industry Applications Conference, 2003.38th IAS Annual Meeting*, Vol. 3 (2003) pp. 1918–1925.

[3] A. Boglietti, C. Gerada, and A. Cavagnino, *High-speed electrical machines and drives [special section intro.],* Industrial Electronics, IEEE Transactions **61**, 2943 (2014).

[4] A. M. EL-Refaie, *Fractional-slot concentrated-windings synchronous permanent magnet machines: Opportunities and challenges,* Industrial Electronics, IEEE Transactions **57**, 107 (2010).

[5] B. Funieru and A. Binder, *Simulation of electrical machines end effects with reduced length 3d fem models,* in *Electrical Machines (ICEM), 2012 XXth International Conference* (2012) pp. 1430–1436.

[6] M. R. Shah and A. M. EL-Refaie, *End effects in multiphase fractional slot concentrated-winding surface permanent magnet synchronous machines,* Energy Conversion, IEEE Transactions **25**, 1001 (2010).

[7] P. Handgruber, A. Stermecki, O. Biro, A. Belahcen, and E. Dlala, *Three-dimensional eddy-current analysis in steel laminations of electrical machines as a contribution for improved iron loss modeling,* Industry Applications, IEEE Transactions **49**, 2044 (2013).

[8] L. Cheng-Tsung, L. Hsiu-Ying, and H. Chang-Chou, *A rational iron loss assessment scheme for electromagnetic steel products,* Magnetics, IEEE Transactions **48**, 2993 (2012).

[9] G. Vogt, R. Romary, G. Parent, and V. Costan, *Study of stator core-end packets under the action of two incident fluxes — real scale model,* in *IECON 2012 - 38th Annual Conference on IEEE Industrial Electronics Society* (2012) pp. 2043–2048.

[10] K. Shima, T. Murai, T. Fukami, Y. Furukawa, and A. Komura, *Measurement and analysis of in-plane eddy current in lamination steel using a new tester,* in *Electrical Machines (ICEM), 2012 XXth International Conference* (2012) pp. 1771–1777.

[11] K. Yamazaki, S. Tada, H. Mogi, Y. Mishima, C. Kaido, S. Kanao, K. Takahashi, K. Ide, K. Hattori, and A. Nakahara, *Eddy current analysis considering lamination for stator core ends of turbine generators,* IEEE Transactions on Magnetics **44**, 1502 (2008).

[12] E. Schmidt, G. Traxler-Samek, and A. Schwery, *Influence of higher harmonics in the end region magnetic field on eddy currents in the stator clamping system of hydro generators,* in *Electric Machines and Drives, 2005 IEEE International Conference on* (2005) pp. 1268–1274.

[13] G. Bertotti, *Hysteresis in Magnetism* (Academic Press, San Diego, 1998).

[14] Y. Zhang, M.-C. Cheng, and P. Pillay, *Magnetic characteristics and excess eddy current losses.* in *IAS* (IEEE, 2009) pp. 1–5.

[15] I. Mayergoyz and C. Serpico, *Nonlinear diffusion of electromagnetic fields and excess eddy current losses,* Journal of Applied Physics **85** (1999).

[16] C. Serpico, C. Visone, I. D. Mayergoyz, V. Basso, and G. Miano, *Eddy current losses in ferromagnetic laminations,* Journal of Applied Physics **87** (2000).

[17] Y. Chen and P. Pillay, *An improved formula for lamination core loss calculations in machines operating with high frequency and high flux density excitation,* in *Industry Applications Conference, 2002. 37th IAS Annual Meeting. Conference Record of the*, Vol. 2 (2002) pp. 759–766 vol.2.

[18] D. M. Ionel, M. Popescu, S. J. Dellinger, T. J. E. Miller, R. J. Heideman, and M. I. McGilp, *On the variation with flux and frequency of the core loss coefficients in electrical machines,* IEEE Transactions on Industry Applications **42**, 658 (2006).

[19] M. Popescu and D. M. Ionel, *A best-fit model of power losses in cold rolled-motor lamination steel operating in a wide range of frequency and magnetization,* IEEE Transactions on Magnetics **43**, 1753 (2007).

[20] M. Ibrahim and P. Pillay, *Advanced testing and modeling of magnetic materials including a new method of core loss separation for electrical machines,* IEEE Transactions on Industry Applications **48**, 1507 (2012).

[21] G. R. Slemon and X. Liu, *Core losses in permanent magnet motors,* IEEE Transactions on Magnetics **26**, 1653 (1990).

[22] C. Mi, G. R. Slemon, and R. Bonert, *Modeling of iron losses of permanent-magnet synchronous motors,* IEEE Transactions on Industry Applications **39**, 734 (2003).

[23] W. Roshen, *Iron loss model for permanent-magnet synchronous motors,* IEEE Transactions on Magnetics **43**, 3428 (2007).

[24] S. E. Zirka, Y. I. Moroz, P. Marketos, and A. J. Moses, *Loss separation in nonoriented electrical steels,* IEEE Transactions on Magnetics **46**, 286 (2010).

[25] J. Gyselinck, L. Vandevelde, J. Melkebeek, P. Dular, F. Henrotte, and W. Legros, *Calculation of eddy currents and associated losses in electrical steel laminations,* IEEE Transactions on Magnetics **35**, 1191 (1999).

[26] R. Stoll, *The analysis of eddy currents* (Clarendon Press, Oxford, 1974).

[27] T. L. Mthombeni and P. Pillay, *Physical basis for the variation of lamination core loss coefficients as a function of frequency and flux density,* in *IECON 2006 - 32nd Annual Conference on IEEE Industrial Electronics* (2006) pp. 1381–1387.

[28] J. R. Brauer, Z. J. Cendes, B. C. Beihoff, and K. P. Phillips, *Laminated steel eddy current loss versus frequency computed using finite elements,* in *Electric Machines and Drives, 1999. International Conference IEMD '99* (1999) pp. 543–545.

[29] J. Pippuri, A. Belahcen, E. Dlala, and A. Arkkio, *Inclusion of eddy currents in laminations in two-dimensional finite element analysis,* IEEE Transactions on Magnetics **46**, 2915 (2010).

[30] E. Dlala and A. Arkkio, *A general model for investigating the effects of the frequency converter on the magnetic iron losses of a squirrel-cage induction motor,* IEEE Transactions on Magnetics **45**, 3303 (2009).

[31] Bottauscio, O., Chiampi, M., Manzin, A., and Zucca, M., *Prediction of losses in induction machines: a challenge for the modelling approaches,* Eur. Phys. J. Appl. Phys. **30**, 7 (2005).

[32] A. G. Jack and B. C. Mecrow, *Calculation of three-dimensional electromagnetic fields involving laminar eddy currents,* IEE Proceedings A - Physical Science, Measurement and Instrumentation, Management and Education - Reviews **134**, 663 (1987).

[33] V. C. Silva, G. Meunier, and A. Foggia, *A 3d finite-element computation of eddy currents and losses in the stator end laminations of large synchronous machines,* Magnetics, IEEE Transactions **32**, 1569 (1996).

[34] O. Bíró, K. Preis, and I. Ticar, *A fem method for eddy current analysis in laminated media,* COMPEL - The international journal for computation and mathematics in electrical and electronic engineering **24**, 241 (2005).

[35] K. Muramatsu, T. Okitsu, H. Fujitsu, and F. Shimanoe, *Method of nonlinear magnetic field analysis taking into account eddy current in laminated core,* IEEE Transactions on Magnetics **40**, 896 (2004).

[36] J. Gyselinck, R. V. Sabariego, and P. Dular, *A nonlinear time-domain homogenization technique for laminated iron cores in three-dimensional finite-element models,* IEEE Transactions on Magnetics **42**, 763 (2006).

[37] K. Hollaus, *Estimation of 3d eddy currents in conduction laminations by an anisotropic conductivity and a 1D analytical solution*, Ph.D. thesis, University of Technology of Graz (2001).

[38] K. Hollaus and O. Biro, *A fem formulation to treat 3d eddy currents in laminations,* IEEE Transactions on Magnetics **36**, 1289 (2000).

[39] T. Chevalier, A. Kedous-Lebouc, and B. Cornut, *Influence of electrical sheet width on dynamic magnetic properties,* Journal of Magnetism and Magnetic Materials **215–216**, 623 (2000).

[40] O. Bottauscio, M. Chiampi, and D. Chiarabaglio, *Magnetic flux distribution and losses in narrow ferromagnetic strips,* Journal of Magnetism and Magnetic Materials **215–216**, 46 (2000).

[41] K. Hollaus, M. Huber, J. Schöberl, and P. Hamberger, *A linear fem benchmark for the homogenization of the eddy currents in laminated media in 3d,* IFAC Proceedings Volumes **45**, 1190 (2012).

[42] A. D. Rochebrune, J. M. Dedulle, and J. C. Sabonnadiere, *A technique of homogenization applied to the modelling of transformers,* IEEE Transactions on Magnetics **26**, 520 (1990).

[43] P.-S. Shin and J. Lee, *Magnetic field analysis of amorphous core transformer using homogenization technique,* IEEE Transactions on Magnetics **33**, 1808 (1997).

[44] K. R. Shao, K. D. Zhou, and J. D. Lavers, *Boundary element analysis method for 3-d multiply connected eddy current problems based on the second order vector potential formulation,* IEEE Transactions on Magnetics **28**, 1216 (1992).

[45] T. P. Theodoulidis, N. V. Kantartzis, T. D. Tsiboukis, and E. E. Kriezis, *Analytical and numerical solution of the eddy-current problem in spherical coordinates based on the second-order vector potential formulation,* IEEE Transactions on Magnetics **33**, 2461 (1997).

[46] C. Emson, J. Simkin, and C. Trowbridge, *Further developments in three dimensional eddy current analysis,* IEEE Transactions on Magnetics **21**, 2231 (1985).

[47] P. Dular, J. Gyselinck, C. Geuzaine, N. Sadowski, and J. P. A. Bastos, *A 3-d magnetic vector potential formulation taking eddy currents in lamination stacks into account,* IEEE Transactions on Magnetics **39**, 1424 (2003).

[48] L. Krahenbuhl, P. Dular, T. Zeidan, and F. Buret, *Homogenization of lamination stacks in linear magnetodynamics,* IEEE Transactions on Magnetics **40**, 912 (2004).

[49] K. Hollaus, A. Hannukainen, and J. Schöberl, *Two-scale homogenization of the nonlinear eddy current problem with fem,* IEEE Transactions on Magnetics **50**, 413 (2014).

[50] S. Nogawa, M. Kuwata, T. Nakau, D. Miyagi, and N. Takahashi, *Study of modeling method of lamination of reactor core,* IEEE Transactions on Magnetics **42**, 1455 (2006).

[51] K. Preis, O. Biro, and I. Ticar, *Fem analysis of eddy current losses in nonlinear laminated iron cores,* IEEE Transactions on Magnetics **41**, 1412 (2005).

[52] H. D. Gersem, S. Vanaverbeke, and G. Samaey, *Three-dimensional - two-dimensional coupled model for eddy currents in laminated iron cores,* IEEE Transactions on Magnetics **48**, 815 (2012).

[53] J. Wang, H. Lin, Y. Huang, and L. Huang, *Numerical analysis of 3d eddy current fields in laminated media under various frequencies,* IEEE Transactions on Magnetics **48**, 267 (2012).

[54] S. Urata, M. Enokizono, T. Todaka, and H. Shimoji, *Magnetic characteristic analysis of the motor considering 2-d vector magnetic property,* IEEE Transactions on Magnetics **42**, 615 (2006).

[55] M. Bali, H. D. Gersem, and A. Muetze, *Finite-element modeling of magnetic material degradation due to punching,* IEEE Transactions on Magnetics **50**, 745 (2014).

[56] S. Steentjes, G. von Pfingsten, and K. Hameyer, *An application-oriented approach for consideration of material degradation effects due to cutting on iron losses and magnetizability,* IEEE Transactions on Magnetics **50**, 1 (2014).

[57] H. Hamzehbahmani, P. Anderson, K. Jenkins, and M. Lindenmo, *Experimental study on interlaminar short-circuit faults at random positions in laminated magnetic cores,* IET Electric Power Applications **10**, 604 (2016).

[58] J. H. J. Potgieter and M. J. Kamper, *Calculation methods and effects of end-winding inductance and permanent-magnet end flux on performance prediction of nonoverlap winding permanent-magnet machines,* IEEE Transactions on Industry Applications **50**, 2458 (2014).

[59] *Comsol multiphysics® v. 4.4b,* COMSOL AB, Stockholm, Sweden.

A

Ferromagnetic materials

Core laminations are made from ferromagnetic materials such as iron (Fe), nickel (Ni) and their alloys. When placed in a magnetic field, ferromagnetic materials are strongly magnetized in the direction of the magnetic field. This makes those materials excellent for guiding flux in electrical machines.

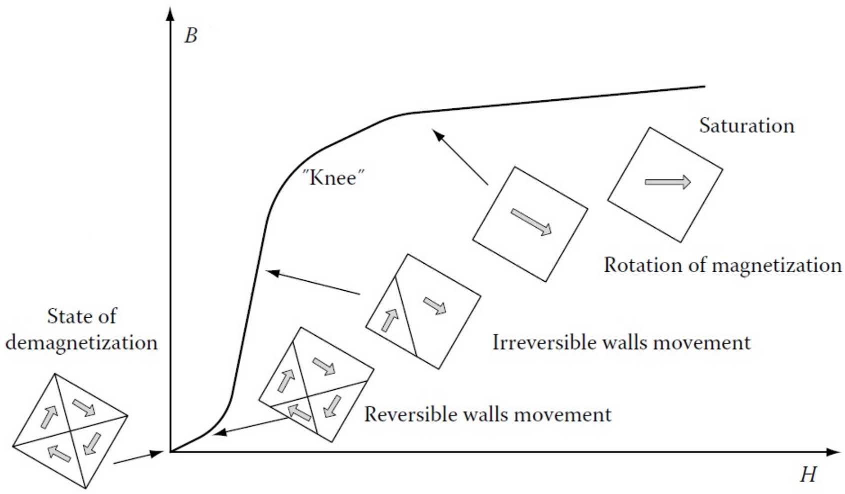

Figure A.1: A typical magnetization curve of a ferromagnetic material

Magnetic material spontaneously creates small regions of the same direction of magnetization, magnetic domains, in order to ensure minimum free energy. Domain walls separate any domains of opposite direction of magnetization. In these domain wall, normally thinner than 10μm, the magnetic dipoles reverse their alignment. The existence of those magnetic domains and domain walls influence the process of magnetization significantly. While increasing the field strength, the process of magnetization is shown in figure A.1 and can be divided into the following characteristic parts.

1. State of demagnetization
2. Reversible walls movements
3. Irreversible walls movement
4. Rotation of magnetization
5. Saturation

applying a magnetic field on a fully demagnetized sample[1], the domains with magnetization closest to the direction of the magnetic field starts to grow at the expense of other domains. For small

[1]Full demagnetization can be reached by placing the sample in a large alternating field and slowly decrease the amplitude of this field to zero.

magnetic fields this process is reversible and there will be no hysteresis effects. The irreversible wall movement state is reached when applying larger magnetic fields and is characterised by the maximum permeability. If the magnetic field is now removed, the material stays partly magnetized due to the new positions of the domain walls; the hysteresis effect starts to appear. Increasing the magnetic field even further, above the knee point, the magnetic field tries to force the directions of magnetizations along the direction of this field. The change of the magnetic flux with increasing magnetic field strength is now much smaller. The saturation state is reached when the directions of magnetizations and the magnetic field are aligned.

Hysteresis Loop

The hysteresis is a behavior characteristic practically for all ferromagnetic materials and appeared from the moment the irreversible walls movement state is reached by the domain walls. A typical hysteresis loop is shown in figure A.2. In this figure, B_r is the residual or remanent flux density that remains in the material at zero magnetic field strength. To reach zero flux density , a field in the opposite direction needs to be applied; this field is called coercivity H_c. A varying magnetic field causes the material to cycle through hysteresis curve. The magnetic core loss depends on the area of the hysteresis loop.

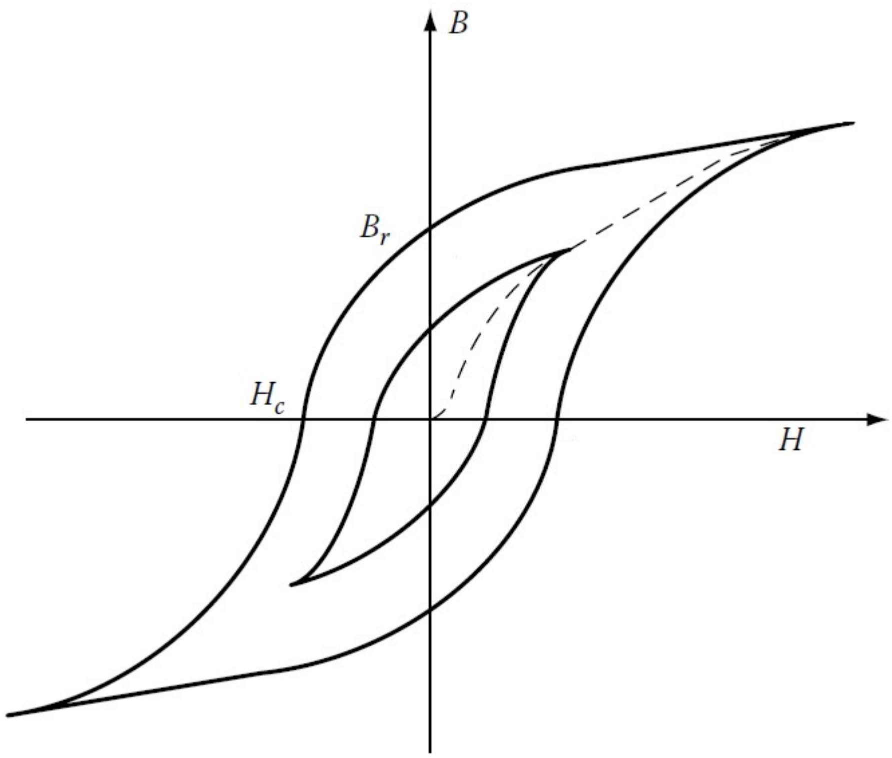

Figure A.2: A typical hysteresis curve of a ferromagnetic material

The hysteresis loop or static loop is normally measured at low frequencies, where eddy currents induced in the core are negligible small. Higher frequencies cause the B-H loop to broaden due to the pronounced effect of eddy currents induced in the core. This enlarged loop is called hystero-eddy current loop or dynamic loop.

B

Additional 3D FEM models

In this appendix two additional models are shown. Figure B.1 and Figure B.2 show a model without end-winding and with extended end-winding, respectively. The modelled results are compared with the original simplified model in chapter 4.

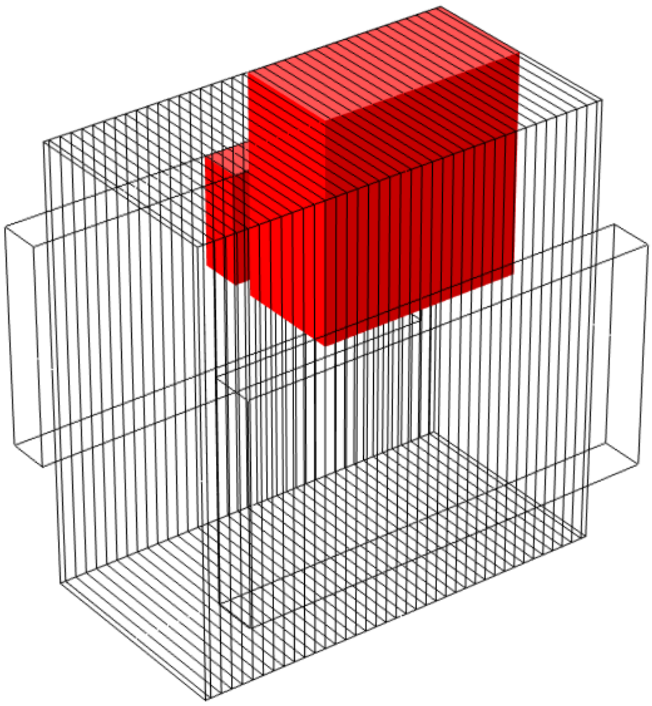

Figure B.1: Simplified 3D model with no end-winding

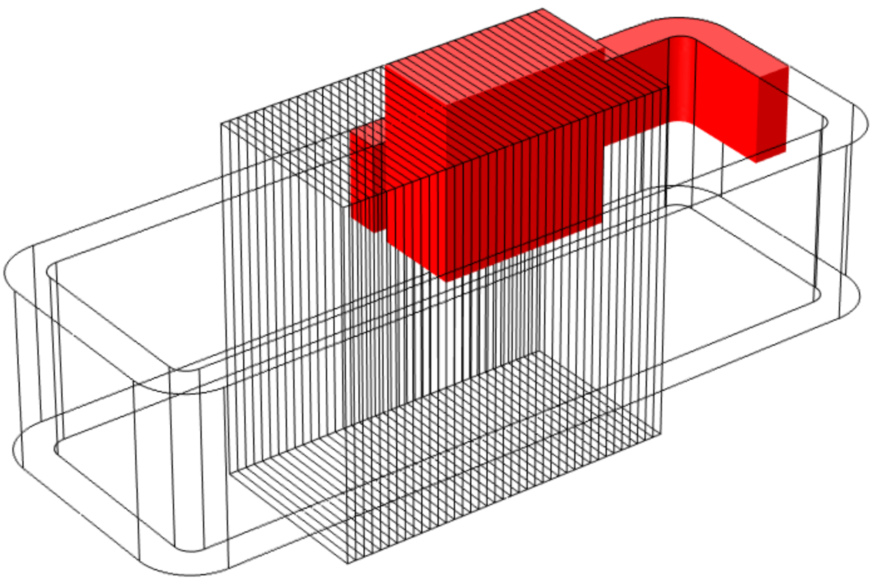

Figure B.2: Simplified 3D model with extended end-winding

C

Additional 3D FEM results

In this appendix the results are presented of the simplified 3D model with a conductivity of $3e7\ S/m$. Figure C.1 and Figure C.2 shows the magnetic flux distribution and current density distribution, respectively. The results for the cut lines described in Chapter 4 are give in Figure C.3, Figure C.4, Figure C.5 and Figure C.6. The eddy-current losses are much higher than the original 3D model and the skin effect emerges already at low frequencies.

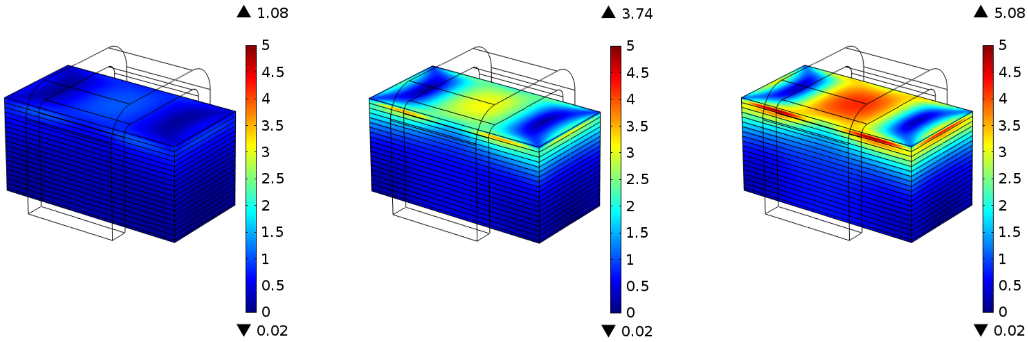

Figure C.1: Magnetic flux density (T) distribution for 50 Hz (left), 500 Hz (middle) and 1 kHz (right)

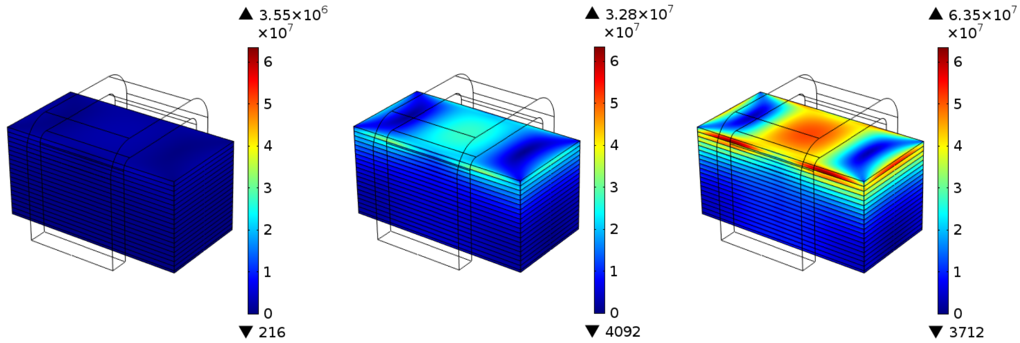

Figure C.2: Induced current density (A/m^2) distribution for 50 Hz (left), 500 Hz (middle) and 1 kHz (right)

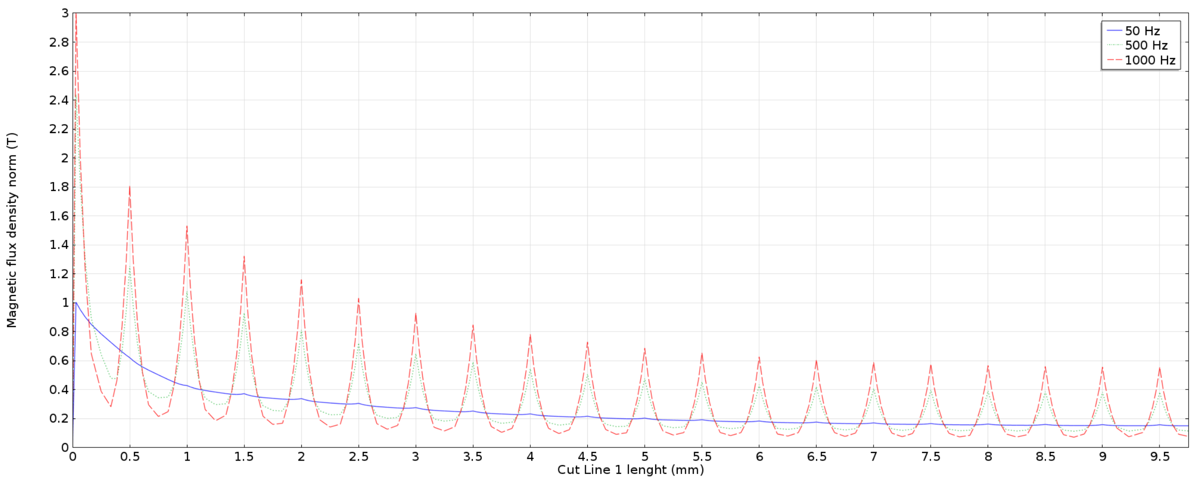

Figure C.3: Magnetic flux density along cut line 1

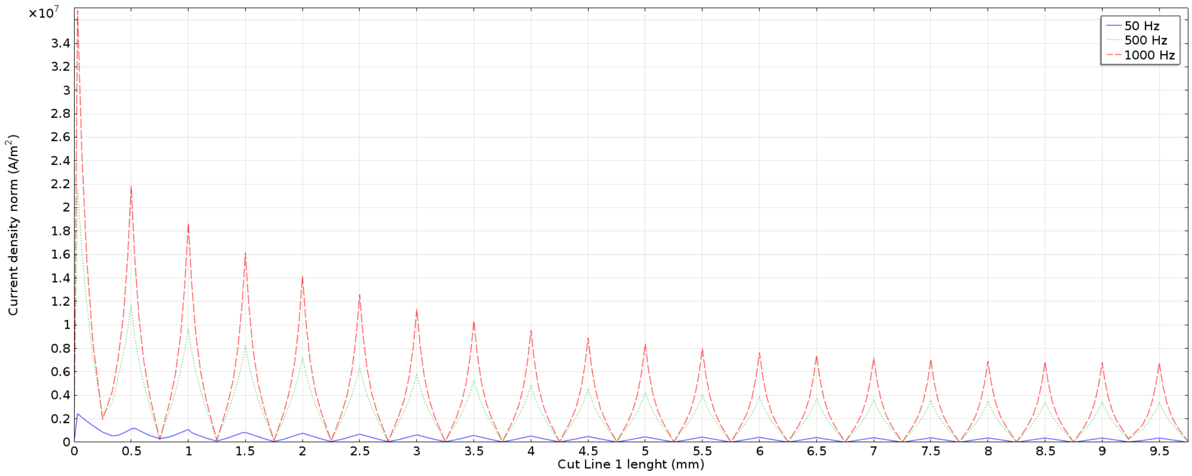

Figure C.4: Current density along cut line 1

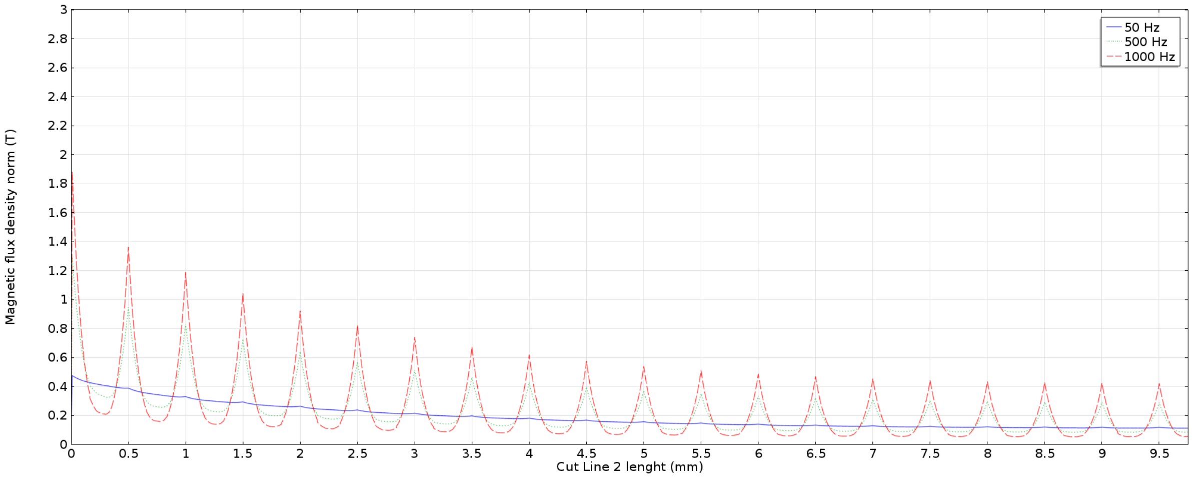

Figure C.5: Magnetic flux density along cut line 2

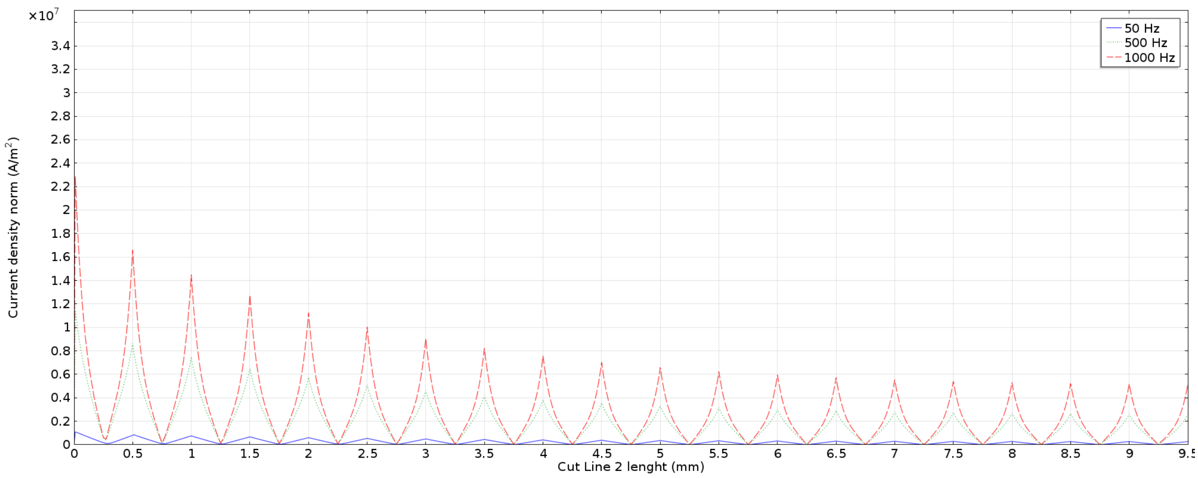

Figure C.6: Current density allong cut line 2